Graduating university
Ministry of Science and Higher Education of the Russian Federation
National Research Tomsk Polytechnic University
School of Nuclear Science & Engineering

Guiding firm
Czech Academy of Sciences
Nuclear Physics Institute
Nuclear Spectroscopy Department

Study of hadron-jet correlations in high-multiplicity pp collisions at $\sqrt{s} = 13$ TeV

By Artem Yu. Kotliarov

A graduation work
Submitted in fulfillment of the
graduation work requirements
for master's degree

Approved by:
Supervisor (NPI): Křížek Filip, RNDr., Ph.D.
Science advisor (TPU): Andrey Yu. Trifonov, D. Sc.

Řež near Prague, Tomsk – 2020

Acknowledgments

In the first place, I would like to express my sincere gratitude to my supervisor, **RNDr. Křížek Filip, Ph.D.**, for his patience and invaluable contribution to the preparation of the diploma thesis, as well as for help in passing the entrance exam of the Ph.D. programme. I am immensely grateful to **Křížek Filip** for introducing me to the new topic as well for the support on the way. **Peter Martin Jacobs** from the Lawrence Berkeley National Lab. (US) also deserves my gratitude for his comments.

Special thanks to the management of the Nuclear Physics Institute of the Czech Academy of Sciences and, in particular, to **Svetlana Kushpil, CSc.**, who has made possible my internship in the institute.

Finally, I would like to thank to my family for their love, understanding, and support.

Bc. Artem Kotliarov

Contents

Introduction

The nuclear matter is changed under extreme conditions to the Quark-Gluon Plasma (QGP) phase, in which quarks and gluons escape their confinement in hadrons. In order to study QGP in laboratory conditions, ultra-relativistic heavy-ion collisions are used, which allow us to achieve large energy densities and temperatures in a finite volume. As the collision zone expands and cools, quarks and gluons merge together giving rise to a multitude of hadrons which further interact among each other until the *kinetic freeze-out* stage is reached [1]. When particles from the collision reach detectors, the QGP does not exist any more, therefore its properties can be investigated utilising only indirect approaches. Among different experimental observables that are studied in this context, two of them are believed to be directly associated with the production of the QGP in heavy-ion collisions: the large azimuthal-momentum space anisotropy of the final state particles [2] and the jet quenching phenomenon [3]. The first observable is connected with the time evolution of the initial spatial anisotropy of the collision zone, that results in an azimuthal-momentum space anisotropy of produced particles. Hydrodynamic calculations, which model this process, show that the magnitude of the observed flow is compatible with QGP behaving like a nearly perfect liquid with a small shear viscosity to entropy-density ratio [4].

The jet quenching phenomenon is manifested by a remarkable reduction of energy of high-p_{T} hadrons and jets which traversed the QGP medium. Their yield measured in heavy-ion collisions is suppressed when compared to the yield that would be expected from a superposition of the corresponding number of independent p+p collisions.

Recently, flow-like signatures were observed also in smaller systems such as p+Pb [5] and p+p. Thus, it is natural to ask whether this is evidence that the QGP is produced in small systems and whether quenching of jets should be also seen.

In 2016–2018, the ALICE experiment at the CERN LHC, collected a large statistics of p+p collisions at $\sqrt{s}$ = 13 TeV. The data were selected with a high-multiplicity trigger (HM) as well as with a reference minimum bias trigger (MB). The HM trigger is expected to select events with an enhanced number of multipartonic interactions. Such events could possibly form a droplet of QGP. These data were used for studying of medium-induced acoplanarity in hadron-jet system. Obtained results

showed marked suppression of back-to-back correlation in hadron-jet systems for high multiplicity events w.r.t. minimum bias events [6]. Such suppression is a signature of the jet quenching effect. Later, embedding studies, using the PYTHIA event generator [7], had excluded the possibility that the observed suppression would be caused by inefficient jet reconstruction in a high-multiplicity environment. Therefore, the observed suppression has a physical nature.

Additionally, hadron-jet acoplanarity was studied in events simulated with PYTHIA 8 events generator. It was shown, that PYTHIA simulations exhibit qualitatively the same suppression feature [6]. This fact suggests that observed suppression is not the result of jet quenching effect, since the last is not implemented into the PYTHIA generator. However, since PYTHIA reproduces the effect, it can be utilised to search for origin of the observed phenomenon.

to trace down the origin of the suppression seen in PYTHIA

The primary goal of this diploma thesis is to trace down the origin of the suppression seen in PYTHIA p+p collisions at $\sqrt{s} = 13$ TeV. To achieve this goal, one should:

- get familiar with the basics of Quantum Chromodynamics and phase diagram of strongly interacting matter;
- study what is a jet, how a jet is produced and how a jet reconstruction is performed;
- get familiar with a hadron-jet correlation technique;
- study of what is the PYTHIA 8 event generator, which capabilities it provides;
- generate PYTHIA events and investigate them by means of hadron-jet correlation technique;
- draw a conclusion regarding the obtained results.

The thesis is organised as follows. Chapter 1 gives a brief introduction to quantum chromodynamics (QCD). This part describes the main QCD properties, as well as the phase diagram of strongly interacting matter. Further, we discuss how such extreme states of matter can be probed with ultrarelativistic heavy-ion collisions. Chapter 2 gives a basic concept of a jet, how jet reconstruction is performed and how the quenching effect modifies jet properties. Chapter 3 contains a brief description of jet reconstruction in the ALICE experiment and detectors, which are used for that. Chapter 4 contains overview of the results of hadron-jet acoplanarity studies

in real p+p collisions at $\sqrt{s} = 13$ TeV. Chapter 5 presents my analysis of hadron-jet correlation in p+p 13 TeV events simulated by the PYTHIA Monte Carlo event generator. The last chapter then summarises the achieved results.

1 Introduction to Quantum Chromodynamics

1.1 Quark model

The strong interaction is one of the four fundamental interactions that can be found in nature. Its discovery dates back to the early 1930s, when the interaction between protons and neutrons was realised as a new kind of force. Experiments have shown, that the interaction is powerful (roughly 10^2 times greater than the electromagnetic force) and that it acts only at short distances. First attempts to describe the strong interaction were done by H. Yukawa [8]. He assumed, that the interaction between nucleons is mediated by a charged, heavy boson, a so-called π-meson. The theory was confirmed when π-mesons were observed as free particles in cosmic rays and in accelerator experiments in the 1940s [9].

In the mid 1960s, particle physics was progressing by development of accelerator and detector technologies. The existence of a large number of strongly interacting particles served as evidence of a composite character of hadrons. The Yukawa theory was found to be only an effective theory.

An important breakthrough was achieved, when it was realized that known hadrons could be sorted into groups according to their quantum numbers and that structuring of these groups exhibits symmetries. M. Gell-Mann and Y. Ne'eman proposed that known hadrons could be classified in terms of multiplets of the Lie group SU(3), which is based on three elementary generators which were noted as *u*, *d* and *s* [10, 11]. Gell-Mann called them *quarks*. Quarks were proposed to be spin 1/2 particles with fractional elementary electrical charges.

In the quark model, quantum numbers of hadrons are determined by their constituent quarks and antiquarks. The quark model was successful in the predictions of the relations between magnetic moments of hadrons [12]. Also, it predicted the existence of the Ω^- baryon (with the quark content *sss*) which is a member of the decuplet. However, the model had also drawbacks: some quark combinations, that the model predicted, violated the Pauli exclusion principle (e.g. the above mentioned Ω^-) and the model did not say what holds quarks inside hadrons together. These issues were resolved later by introducing the colour charge and by the discovery of quantum chromodynamics (QCD) [13].

Table 1.1 – Additive quantum numbers of quarks

	d	u	s	c	b	t
Q - electric charge	$-\frac{1}{3}$	$+\frac{2}{3}$	$-\frac{1}{3}$	$+\frac{2}{3}$	$-\frac{1}{3}$	$+\frac{2}{3}$
I_3 - isospin projection	$-\frac{1}{2}$	$\frac{1}{2}$	0	0	0	0
S - strangeness	0	0	-1	0	0	0
C - charm	0	0	0	+1	0	0
B - bottomness	0	0	0	0	-1	0
T - topness	0	0	0	0	0	+1

Nowadays we know about six flavours of quarks. Their additive quantum numbers are shown in Table 1.1. In addition, each quark has the additive *baryon* number $\mathfrak{B} = 1/3$. All ordinary hadrons can be obtained by combining $3q$ (baryons) or $q\bar{q}$ (mesons) and they can be grouped into the decuplet, octets, and singlets. The *weight diagrams* for mesons and baryons are depicted in Fig. 1.1.

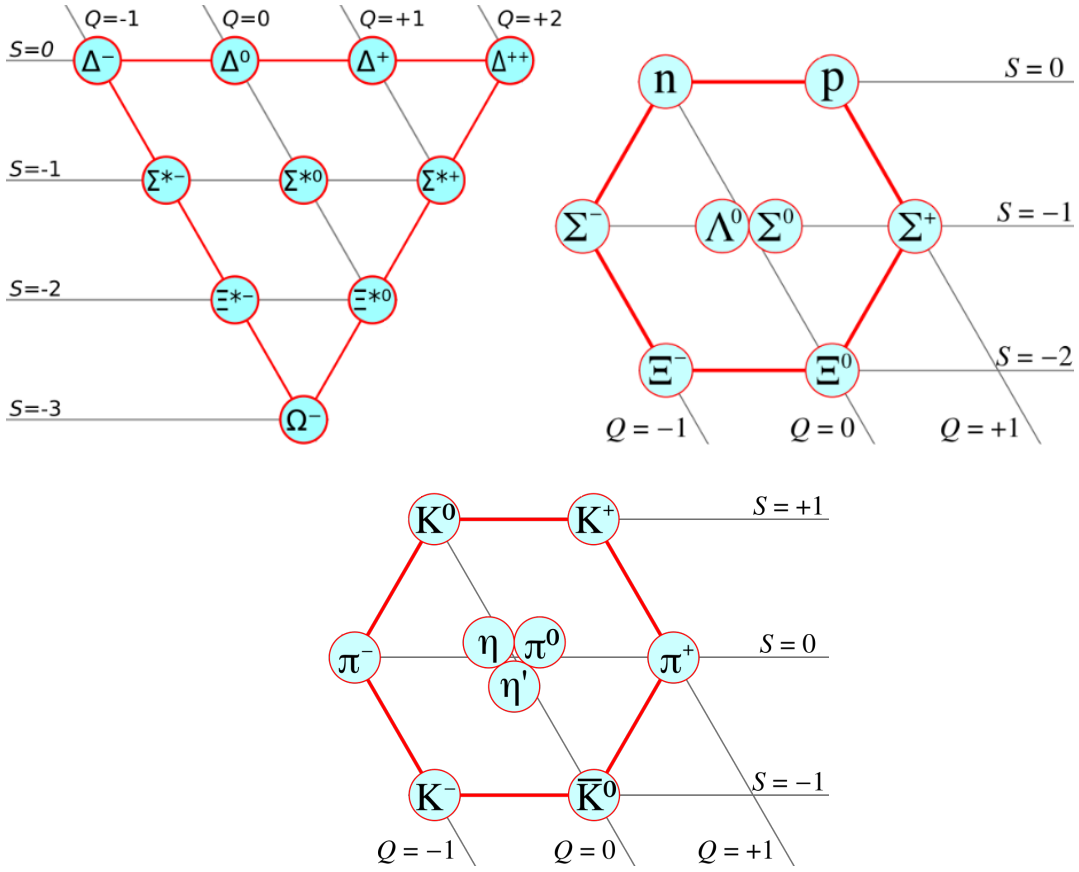

Figure 1.1 – SU(3) weight diagrams. Left: baryon decuplet. Right: baryon octet. Bottom: meson octet + singlet. The Q and S axes give electrical charge and strangeness, respectively, of given hadrons. Taken from [14].

1.2 QCD Lagrangian

The fundamental theory of the strong interaction was discovered in 1973 by F. Wilczek, D.J. Gross and H.D. Politzer [15, 16]. Quantum chromodynamics is a gauge field theory describing interactions between quarks, anti-quarks and gluons. The QCD Lagrangian is designed such that it is invariant under local transformations of colour degrees of freedom. The gauge symmetry group of QCD is the non-Abelian Lie group SU(3). QCD contains eight kind of gluon fields which act as the gauge bosons, mediating the interaction between colour charges. Their number is given by the number of generators of the SU(3) group.

The QCD Lagrangian can be derived from a free fermion field Lagrangian when a local gauge transformation invariant w.r.t. the group SU(3) is imposed [17]:

$$\mathcal{L}_{\mathrm{QCD}}(x) = -\frac{1}{4}\vec{F}^{a}_{\mu\nu}(x)\vec{F}^{a\mu\nu}(x) + \sum_{f=1}^{n_f}\bar{\psi}^{f}_{i}(x)\left[i\gamma^{\mu}\partial_{\mu}\delta^{ij} + g_s\gamma^{\mu}A^{a}_{\mu}t^{aij} - m_f\delta^{ij}\right]\psi^{f}_{j}(x), \tag{1.1}$$

where $\vec{F}^{a}_{\mu\nu} = \left(F^{1}_{\mu\nu}, F^{2}_{\mu\nu}, \ldots, F^{8}_{\mu\nu}\right)$ is a vector of the gluon field tensors, $i, j = (1, 2, 3)$ denote a colour indices and $a = (1, \ldots, 8)$ denotes an adjoint colour index. Lorentz indices are represented by Greek letters and the Einstein summation convention is adopted. The summation goes through all quark flavours. The γ_μ and δ^{ij} are the Dirac matrices and Kronecker symbol, respectively. The $\psi^{f}_{j}(x)$ and $\bar{\psi}^{f}_{i}(x)$ represent a quark and antiquark spinor field operator of flavor f and mass m_f, with $\bar{\psi} = \psi^{\dagger}\gamma^{0}$. Finally, the gluon field tensor $F^{a}_{\mu\nu}$ is given by

$$F^{a}_{\mu\nu}(x) = \partial_{\mu}A^{a}_{\nu}(x) - \partial_{\nu}A^{a}_{\mu}(x) + g_{\mathrm{s}}f_{abc}A^{b}_{\mu}(x)A^{c}_{\nu}(x), \qquad [t_a, t_b] = i f_{abc}t^{c}, \tag{1.2}$$

where ∂_μ is a covariant derivative, A^{a}_{μ} is a gluon field, f_{abc} and t_a are the structure constants and the generators of the SU(3) group, respectively. The bilinear term in (1.2) reflects the non-Abelian character of the theory, thus QCD, in contrast to QED, contains a self-interaction of three and four gluons that is depicted in terms of the Feynman diagrams in Fig. 1.2.

a) b)

Figure 1.2 – Feynman diagrams for gluon self-interaction in QCD: a) 3-gluon vertex; b) 4-gluon vertex. Taken from [14].

1.3 Running coupling constant

The Lagrangian (1.1) is used to calculate cross sections of elementary processes, which involve interactions of particles with colour charge. The cross section can be calculated by means of the perturbative approach in case that the coupling constant $\alpha_s = g_s^2/4\pi$ is less than 1. In QCD, however, α_s changes its size based on the 4-momentum transfer Q^2 which is involved in the given process, i.e. the coupling constant is running [18]. A dependence of the coupling constant α_s on the energy scale Q is shown in Fig. 1.3. Expression for α_s may be calculated from the renormalization

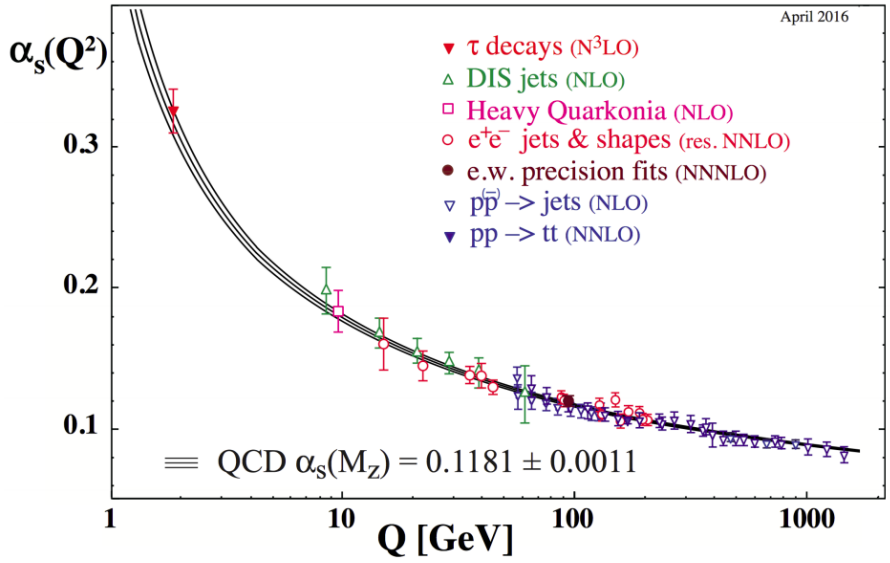

Figure 1.3 – The summary of measurements of the running coupling constant α_s as a function of the energy scale Q. Data from experiments are represented by markers. Prediction of the perturbative QCD and the corresponding uncertainty is shown as the black line and band. The legend also quotes the size of the running coupling constant at the Z boson mass scale. Taken from [19].

group equation (RGE) utilising the beta-function $\beta(\alpha_s)$ [20]:

$$Q^2 \frac{\mathrm{d}\alpha_s}{\mathrm{d}Q^2} = \beta(\alpha_s). \tag{1.3}$$

The QCD has a dimensionful parameter Λ_{QCD} that determines the energy scale where perturbative methods break down. In the leading order (LO) of perturbative theory, relation between α_{s}, Λ_{QCD} and Q^2 can be expressed as [21]

$$\alpha_{\mathrm{s}}(Q^2) = \frac{1}{\beta_0 \ln\left(\frac{Q^2}{\Lambda^2_{\mathrm{QCD}}}\right)}, \tag{1.4}$$

where β_0 is a 1-loop β-function coefficient. Experimental data has shown, that $\Lambda_{\mathrm{QCD}} \approx$ 200 MeV. The strong interaction becomes indeed strong at distances greater than $\sim 1/\Lambda_{\mathrm{QCD}}$, that approximately is equal to the size of the lightest hadrons [18].

Evidently from the equation (1.4), it can be seen that in a process with a large momentum transfer ("hard process") $Q^2 \gg \Lambda^2_{\mathrm{QCD}}$, the coupling constant $\alpha_{\mathrm{s}} \to 0$. Therefore, the interaction between quarks and gluons becomes negligible at asymptotically short distances. This property of QCD is known as the *asymptotic freedom*. It can be seen as an anti-screening effect of the colour charge, i.e. effective colour charge becomes smaller at short distances. This situation is completely opposite for the electric charge screening effect in QED [22].

1.4 Colour confinement

At large distances, QCD exhibits another remarkable property which is known as the *colour confinement*. QCD physical asymptotic states do not involve free quarks and gluons - only colourless states are physical, i.e. hadrons. The confinement is a non-perturbative process and so, at present, beyond our means to calculate it. However, it can be described qualitatively by means of phenomenological models such as the *bag model* of hadrons or the *colour string* model.

Among the different versions of the bag model, the MIT bag model [23] is the most popular one, since it is able to capture most features of the hadron spectra [24]. The model assumes that inside hadrons quarks are massless and outside of hadrons they become infinitely heavy. The model introduces a phenomenological quantity – the bag pressure $\mathcal{B}$, which takes into account non-perturbative effects [25]. The model predicts the following relation between the bag pressure, the number of quarks and hadron radius

$$\mathcal{B}^{1/4} = \frac{1}{R}\left(\frac{2.04N}{4\pi}\right)^{1/4}, \tag{1.5}$$

where N is the number of quarks in a hadron and R is a radius of a hadron. The confinement is described as a result of the balance of the inward bag pressure $\mathcal{B}$ and the expansion arising from the kinetic energy of quarks.

The colour field can span only to the finite distance around the source because gluons, which mediate the strong interaction, possess the colour charge themselves. Thus in the case of mesons, the topology of the colour field can be approximated by a colour flux tube or a colour string which is stretched between the $q\bar{q}$-pair. Based on the observed spectrum of $c\bar{c}$ states, it was found that the interaction potential between the $c\bar{c}$-pair can be described in terms of the Cornell potential [26]:

$$V(r) = -\frac{A}{r} + \sigma r, \tag{1.6}$$

where r is a distance between the colour charges, A is a parameter and σ is a *string tension*. The potential has an attractive coulombic term and a confining term which increases linearly with the distance. The notion of colour string was also very useful when explaining why certain resonances tend to fall on straight lines when we plot a square of their mass M^2 against their full angular momentum J. These lines are known as the *Regge trajectories* [25] (see Fig. 1.4). Such states can be again viewed as

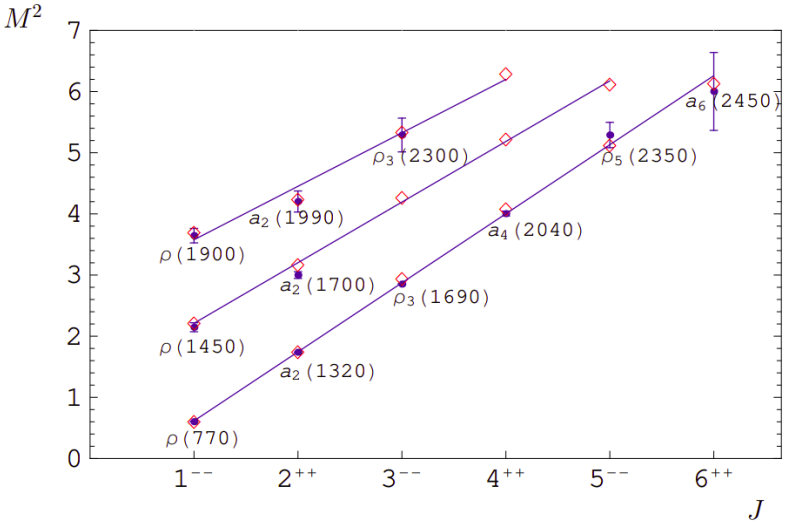

Figure 1.4 – Regge trajectories for isovector light mesons. Diamond markers show predicted masses. Experimental data are given by blue dots with error bars and particle names. The mass is measured in GeV/c^2. Taken from [27].

radial and orbital excitations of a colour string which is stretched between a $q\bar{q}$-pair. The slope of the Regge curves is related to the string tension and is about 1 GeV/fm.

After a hard scattering, the colour strings between particles are being stretched and at some critical moment it is energetically favourable to create a new $q\bar{q}$-pair from

the vacuum. Thereby, the original string is split into smaller string pieces. Location of a vertex, in which the string breaks, can be found by means of the Lund string model [28]. Basic assumption of the model is that vertices lie close to a curve of constant proper time. The field between quark and antiquark created in the same vertex is absent, thus a quark q_j from the vertex V_j will combine with an antiquark $\bar{q}_{j+1}$ from a nearby vertex V_{j+1}. A sketch of Lund string break-up is depicted in Fig. 1.5.

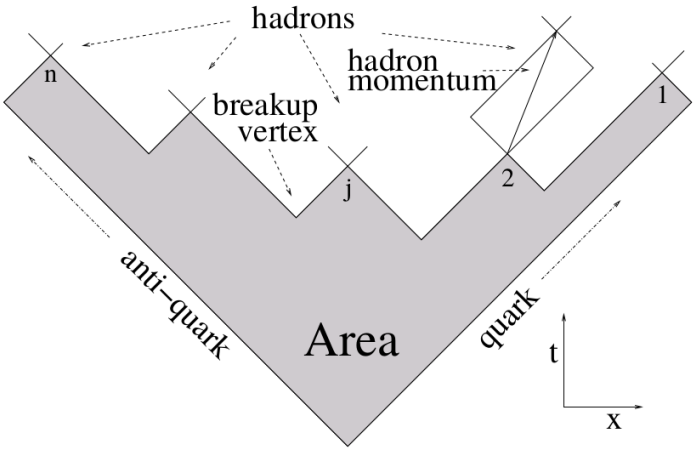

Figure 1.5 – The break-up of Lund string between $q\bar{q}$-pair in space-time. The fragmentation area is labelled as "Area" and shows the area spanned by the string state before it decays (or the total area is equal to transverse mass of produced hadrons). Taken from [28].

1.5 Pseudorapidity variable

For any observed particle of momentum $\mathbf{p}$, energy E, the momentum can be decomposed into components transverse (p_{T}) and longitudinal (p_{L}) to the collision axis. The longitudinal momentum is conveniently expressed in terms of the rapidity y variable:

$$y = \ln\left[\frac{E + p_{\mathrm{L}}}{\sqrt{m^2 + p_{\mathrm{T}}^2}}\right]. \tag{1.7}$$

It is observed, that rapidity distribution $\mathrm{d}N/\mathrm{d}y$ of the final state particles in high energy collisions has a plateau shape [29]. This shape can be described in the frame of the Lund model. In high energy collisions, the speed of particles is close to the speed of light and all produced vertices almost fall on a curve of constant proper time. In this case, rapidity distribution of produced particles can be considered as independent of a rapidity, thus $\mathrm{d}N/\mathrm{d}y$ will be a constant [25]. However, the Lund model cannot predict the full shape of the distribution without additional assumptions.

To characterise the rapidity distribution of particles, it is necessary to measure two kinematic characteristics of a particle. It is more convenient to characterise the detected particles by utilising pseudorapidity variable η (see Fig. 1.6), which is a function of the scattering angle θ:

$$\eta = -\ln[\tan(\theta/2)]. \tag{1.8}$$

In the limit where $\mathbf{p} \to E$ or $m \to 0$, the rapidity reduces to the pseudorapidity η. The conversion from pseudorapidity $\mathrm{d}N/\mathrm{d}\eta$ distribution to rapidity $\mathrm{d}N/\mathrm{d}y$ one is performed by using Jacobian [30]. In experiments at high-energies where $\mathrm{d}N/\mathrm{d}y$ has a plateau shape, this transformation gives a dip around $\eta \approx 0$.

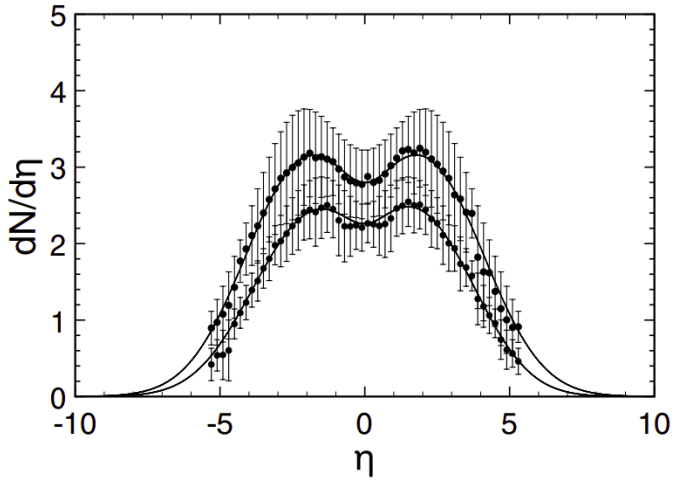

Figure 1.6 – Pseudorapidity distributions of produced charged hadrons in inelastic p+p collisions at RHIC energies of $\sqrt{s} = 0.2$ and 0.41 TeV. Taken from [30].

1.6 QCD phase diagram

The confinement property is inherent to QCD at normal temperatures and nuclear matter densities. In ultrarelativistic heavy-ion collisions, energy densities are so large, that QCD-matter undergoes a phase transition into a new state of asymptotically free quarks, antiquarks and gluons. Such state of matter is called the *quark-gluon plasma* (QGP). One supposes, that QGP must have existed in the primordial Universe about 10^{-10} s to about 10^{-6} s after the Big Bang [24]. Therefore, heavy ion-collisions allow us to recreate a Little bang in laboratory conditions and, thus, study the physics of the early Universe.

Figure 1.7 shows the phase diagram of the QCD-matter as a function of temperature T (vertical axis) and baryo-chemical potential μ_B (horizontal axis). The ordinary nuclear matter is located in the phase diagram at $T \approx 0$ K and $\mu_\mathrm{B} \approx 900$ MeV. When

this matter is heated up, nucleons evaporate from the nucleus and form the so called *hadron gas*. When the hadron gas is further heated up it undergoes a transition to the QGP. As follows from the lattice QCD, close to the temperature axis, the transition

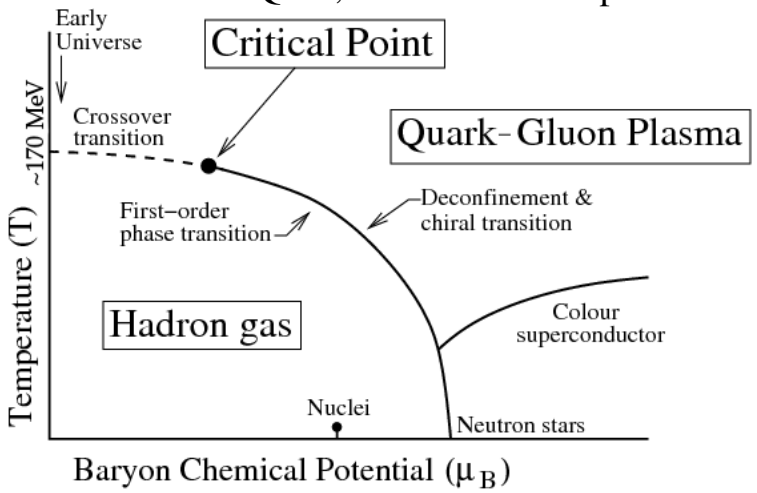

Figure 1.7 – Phase diagram of hot and dense hadronic matter in the temperature and baryo-chemical potential plane. Point "Nuclei" shows the state of the ordinary matter. Taken from [31].

between the QGP and hadron gas proceeds as a rapid *crossover* [32]. The critical temperature T_c and energy densities, required for such a transition, are 156.5 ± 1.5 MeV [33] and $0.2 - 1$ GeV/fm^3 [34], respectively. Due to the sign problem [35], the lattice QCD calculations are not applicable at non-zero values of μ_B. At finite μ_B, one needs to rely on effective models based on the chiral perturbation theory which predict that there is a first order phase transition between the QGP and hadron gas. Thus, at some critical value of baryo-chemical potential μ_B, the crossover turns into a first order phase transition. This point is called the *critical endpoint*. Model calculations [36] predict the existence of the critical point, however, none has succeeded to restrict its location.

The phase diagram also shows what happens to nuclear matter when it is compressed at $T \sim 0$. In this limit hadrons start to overlap, thus quarks and gluons become again weakly coupled. This state of matter is called *cold quark matter*. Such extreme conditions can be reached at the cores of superdense stars such as neutron stars. At very high μ_B one can actually use again pQCD and show, that there is a colour superconductivity state [37].

1.7 Space time evolution of the quark-gluon plasma in heavy-ion collisions

The evolution stages of heavy-ion collisions are shown in Fig. 1.8. In this figure, heavy nuclei collided at $t = 0$. In $\tau_0 \approx 1$ fm/c after the collision, the system

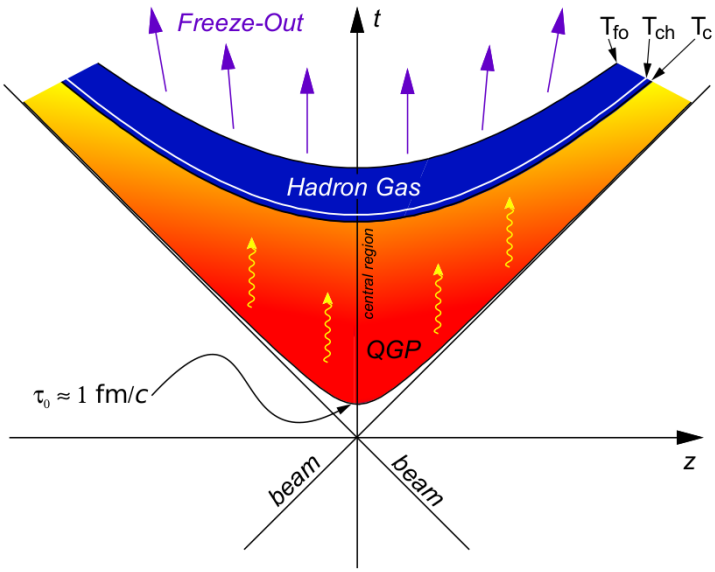

Figure 1.8 – A light cone diagram showing the different stages of a heavy-ion collision. Taken from [38].

goes through a pre-equilibrium phase followed by the formation of a QGP fireball. Its lifetime lasts for about $1 - 10$ fm/c, depending on the collision energy [39]. The system expands and cools rapidly, reaching $T < T_c$ where bound states of quarks and gluons are formed. This stage in the collision evolution is called *hadronization* and corresponds to a phase transition into the hadron gas. As the fireball expands and cools further, the chemical composition of the system is frozen, making the hadron population fixed with time. However, particles interact with each other via elastic scattering. The system has reached the *chemical freeze-out* stage characterized by the temperature T_{ch}. In about 50 fm/c after the collision, the mean free path of the final hadrons becomes greater than the system size, therefore collisions between hadrons cease. From this point, the final energies and momenta of the particles will remain fixed. This stage is called the *kinetic freeze-out*. The associated temperature is labelled as T_{fo}.

Since QGP is a highly unstable system with lifetime of an order of 1 fm/c, it can be investigated only indirectly detecting particles in the final state. In this work, we consider the most prominent QGP signatures: *collective flow* and *jet quenching*. More complete review can be found in [40].

1.8 Collective flow

The QGP behaves like a perfect liquid with shear viscosity lower limit $\eta/s \geq 1/4\pi$ [2]. The strong evidence leading to the discovery of this perfect-liquid behaviour

was found out from the study of the particle collective flow in final state. Since heavy nuclei are finite size objects, the size and shape of the collision region depend on the impact parameter b. A semi-central collision (Fig. 1.9) with a non-zero value of

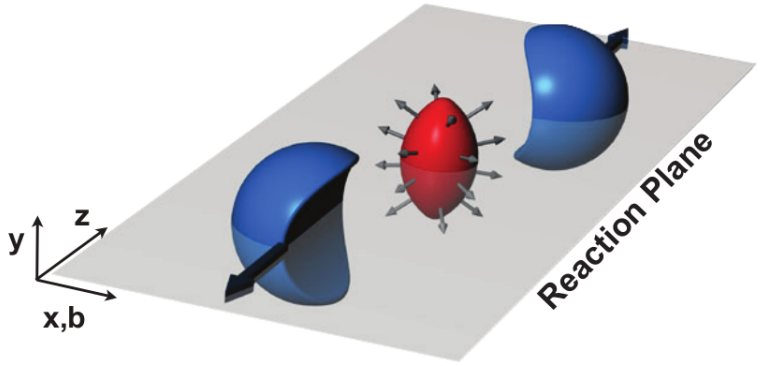

Figure 1.9 – A non-central collision of two nuclei resulting in spatial anisotropy of the overlap region. The spatial anisotropy of energy density w.r.t. the reaction plane leads to the anisotropic flow of particles in the final state. Taken from [41].

the impact parameter results in a spatial asymmetry (almond shape) of the overlap zone. This initial asymmetry evolves into the momentum anisotropy of the final state particles by the hydrodynamical expansion of the created medium. The azimuthal momentum distribution of final state particles can be parameterised by the Fourier expansion of the invariant differential cross section [2]:

$$E\frac{\mathrm{d}^3N}{\mathrm{d}\mathbf{p}^3} = \frac{1}{2\pi}\frac{\mathrm{d}^2N}{p_\mathrm{T}\mathrm{d}p_\mathrm{T}\mathrm{d}y}\left(1+\sum_{n=1}^{\infty}2\upsilon_n\cos[n(\varphi-\Psi_\mathrm{RP})]\right), \tag{1.9}$$

where E, p_T, y and φ are the energy, transverse momentum, rapidity and azimuthal angle of the particles, respectively. Ψ_RP denotes the reaction plane angle. The anisotropic flow coefficients υ_n depend on p_T and y of the particles and they are given by

$$\upsilon_n(p_\mathrm{T},\ y) = \langle\langle\cos[n(\varphi-\Psi_\mathrm{RP})]\rangle\rangle, \tag{1.10}$$

where $\langle\langle\ldots\rangle\rangle$ denotes the double average over all particles in an event and over all events. The first two coefficients υ_1 and υ_2 are known as the *direct* and the *elliptic* flow, respectively.

The magnitude and shape of the leading coefficient $\upsilon_2(p_\mathrm{T})$ can be reproduced by ideal hydrodynamics calculations [42], for particles with transverse momentum $p_\mathrm{T} < (1-2)$ GeV/c, see Fig. 1.10. At p_T above 2 GeV/c, jet fragmentation starts to play a significant role in particle production. Therefore, the measured trend of

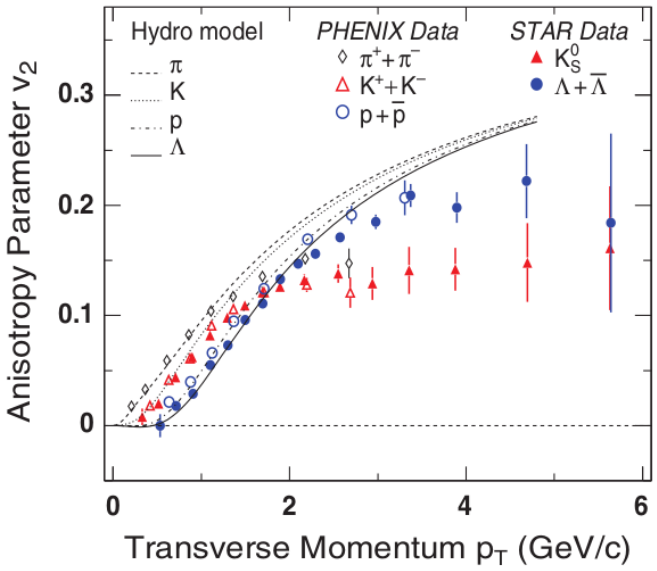

Figure 1.10 – The elliptic flow υ_2 versus p_{T} for π, K, p and Λ, as measured at RHIC and as calculated by an ideal hydrodynamic calculation. Taken from [43]

υ_2 tends to deviate from the hydrodynamical model prediction at high p_{T}. Below 1.5 GeV/c, the hydrodynamical model correctly captures the observed ordering of υ_2 when moving from lighter hadrons to heavier ones.

It was previously thought, that the formation of QGP is only possible in heavy-ion collisions. However, collective phenomena have been recently seen also in small systems such as p+p and p+Pb. Figure 1.11 shows two-particle correlation function for particles with $p_{\mathrm{T}} \in (1, 3)$ GeV/c for different collision systems as a function of azimuthal and pseudorapidity separation. It can be seen, that p+p, p+Pb and Pb+Pb

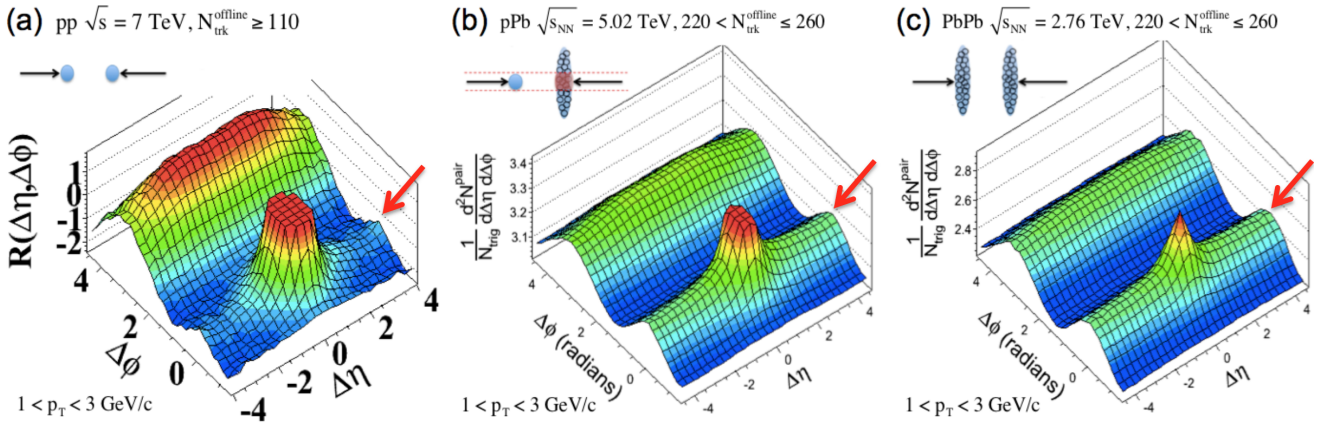

Figure 1.11 – Two-particle correlation function for particles with $p_{\mathrm{T}} \in (1, 3)$ GeV/c in: a) high multiplicity p+p collisions at $\sqrt{s} = 7$ TeV ($N_{\mathrm{trk}}^{\mathrm{offline}} \geq 110$); b) high multiplicity p+Pb collisions at $\sqrt{s} = 5.02$ TeV ($220 < N_{\mathrm{trk}}^{\mathrm{offline}} \leq 260$); c) high multiplicity Pb+Pb collisions at $\sqrt{s} = 2.76$ TeV ($220 < N_{\mathrm{trk}}^{\mathrm{offline}} \leq 260$). Here, $N_{\mathrm{trk}}^{\mathrm{offline}}$ is a track multiplicity determined by offline analysis. Taken from [44, 45, 46].

develop similar “ridge-like” structures (see red arrows in Fig. 1.11) for particles that have small azimuthal separation, but at the same time, have a significant pseudorapidity offset. It is accepted, that such correlation has to be produced early in time. For Pb+Pb collisions, the observed shape results from collision geometry, where spatial anisotropy of the collision zone results to the momentum anisotropy of the final state particles. In p+p, it could be the same effect, but nobody knows for certain. In this situation, it is crucial to look for other QGP signatures in p+p such as jet quenching.

2 Jets

2.1 Concept of a jet

Jets play a crucial role, when we test our understanding of hard QCD processes. Jets provide experimental evidence that collisions of hadrons with a large four-momentum transfer proceed through interactions of quasi-free quarks and gluons, which are generally called partons [47]. Such collisions result in the creation of two or more high-p_{T} partons with large virtuality in the final state. The highly virtual parton emits gluon radiation along its trajectory, which further fragments until one reaches the non-perturbative scale of order Λ_{QCD} or 1 GeV^2. Such process is known as *fragmentation*. The parton branching evolution is governed by the QCD radiation probabilities given by the Dokshitzer–Gribov–Lipatov–Altarelli–Parisi (DGLAP) equations [48]. Newly born partons carry colour charge and due to the colour confinement they must fragment into a set of colourless hadrons in the process called *hadronization*. Eventually, the high-energy partons appear in the final state as a collimated spray of hadrons that is called a *jet*.

The total energy and direction of the jet are quite similar to the initial energy and direction of the parent parton. The matching of the final state jets with initial partons can, however, be ambiguous. Consider a situation, when a parton emits a gluon. If this gluon is emitted at a small angle, it is usually considered as a part of the jet, whereas if it is emitted at a large angle, it may be considered as another jet. Therefore, jet needs to be considered as a phenomenological object defined via algorithm. In the subsequent section, we will discuss this aspect.

2.2 Jets reconstruction

Consistent comparison of theoretical predictions on jet production and jet measurements form experimental data, requires to introduce a *jet definition*, which would establish a set of the rules how jets should be reconstructed from a given list of hadrons in the final state. Typically, a jet definition contains two essential parts. The first one is a *jet algorithm*, i.e. procedure that determines which particles should be grouped during the jet reconstruction. The algorithm is based on a metrics, which calculates how far are particles from each other in an event. The algorithm also decides which particles should be merged or whether the jet is already final. A standard parameter, present in almost all jet algorithms utilised at hadron colliders

is the jet radius R that defines a distance in the rapidity-azimuth ($y - \varphi$) plane above which two particles are no longer considered as a collinear.

The second essential part of a jet definition is a *recombination scheme* that determines the procedure how the kinematic characteristics of a jet are calculated from its constituents. The simplest recombination scheme is the E-scheme which makes a sum of particles' 4-momenta. In addition, there are p_{T} and E_{T} schemes [49], however their use is inconvenient due to their longitudinal non-invariance along the beam axis [50].

At higher orders of pQCD, the quark propagator has two singular regions [51]:

$$\frac{1}{2E_g E_q(1-\beta_q \cos\theta_{qg})} \xrightarrow{E_g \to 0 \text{ or } \theta_{qg} \to 0} \infty, \tag{2.1}$$

where E_q and E_g are the energies of the quark and emitted gluon, respectively, β_q is a speed of the quark in terms of speed of light and θ_{qg} is an angle between quark and emitted gluon. Such divergences are called *infrared* and *collinear*, respectively. In higher order pQCD processes these divergences are cancelled with divergences that appear in loop diagrams. This feature is formulated by the Kinoshita-Lee-Nauenberg theorem [52]: soft and collinear divergences cancel between real and virtual diagrams at any given order of the perturbation theory. A properly designed jet algorithm has to be infrared and collinear safe (IRC) [53]. Only IRC algorithms lead to cancellation of IRC divergences and ensure that the calculated jet cross section is finite. If the

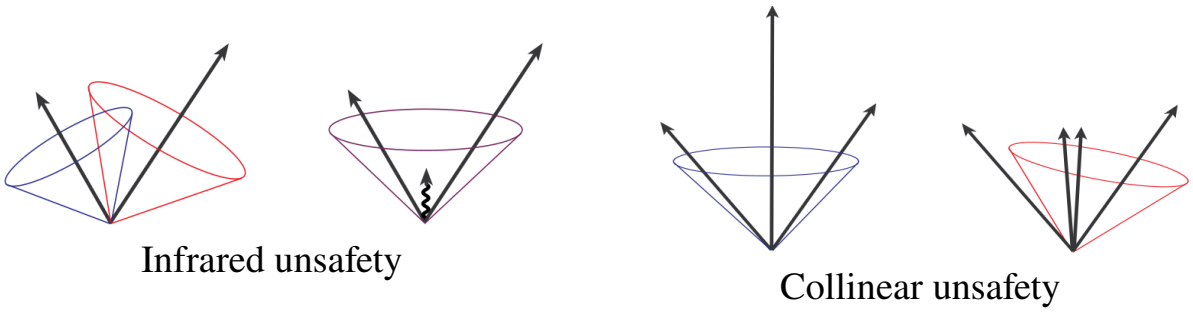

Figure 2.1 – Left: An infrared unsafe algorithm may merge two jets in the presence of soft radiation between them. Right: Collinear splitting of the leading particle, which acts as a seed, may change spatial position of a jet. Taken from [54].

jet algorithm is not IRC safe (see Fig. 2.1), additional soft emission or collinear splitting may lead to unwanted artefacts such as ambiguities in the actual number of jets observed or in their position in phase space.

2.3 Classification of jet algorithms

Over the last decades, a wide variety of jet algorithms has been proposed. They are split into two broad groups: *cone* and *sequential recombination* algorithms. The first of them is based on the assumption that QCD branching and hadronization leave the bulk features of energy flow in event unchanged [55]. Sequential recombination algorithms are designed to sum up radiated energy from a final state parton by repeated merging the closest pair of particles according to some given combining criteria. Further, we shall give more details about the sequential recombination algorithms and briefly discuss the key features of the cone algorithms. The full review can be found in [56].

Usually, jets are divided into the categories according to the parent parton, for instance, gluon jets, light-quark jets or heavy-quark jets (for c, b, t quarks). Also, jets can be distinguished by the particles composition: *charged* and *full* jets. Charged means that jets are reconstructed from charged particles only, whilst full jet also contains neutral particles.

In the LO of pQCD, collisions of two partons lead to 2 jet events, that can be associated with the scattered partons. In reality, since the incoming partons were bound in some hadrons, there have to be 2 additional forward jets resulting from the hadronization of outgoing hadron remnants. Jets are produced with opposite directions in azimuth ($\Delta\varphi \approx \pi$) in their centre of mass system due to the momentum conservation. Such events are more common for elementary collisions and they are called di-jet events. In the next-to-leading order (NLO), highly virtual parton can emit hard gluons which can be recognized as independent jets. Thereby, one can observe three-jet, four-jets and etc. events. Jets formed by primary quarks and gluons, which differ both by their colour charge and spin, have to have different properties [51]:

1. at the same energy, a gluon jet should be on average broader than a quark jet;
2. a multiplicity of any type of particles in a gluon jet is greater than in a quark jet. In the next-to-next-to-leading order (NNLO) calculations, the ratio of constituent multiplicities for gluon and quark jets is equal to $\langle N_g \rangle / \langle N_q \rangle \approx 1.7$. It follows from the fact, that gluon possesses a larger colour charge than a quark.

2.3.1 Cone algorithms

The most widely used cone algorithms are *iterative cones* (IC). The standard scheme of actions of these algorithms is as follows. From the list of final state particles, one chooses a seed particle as the initial direction with rapidity y_i and azimuthal angle φ_i. On the next step, the algorithm evaluates a distance to another particle j using the formula

$$\Delta R^2 = (y_i - y_j)^2 + (\varphi_i - \varphi_j)^2, \tag{2.2}$$

where R is a cone radius. If $\Delta R < R$, the 4-momenta of particles are summed and the resulting direction is utilised as a new seed. If the 4-momentum of the sum has the rapidity y_c and azimuth φ_c, coinciding with the cone centre, the cone is labelled *stable* and the iterative procedure finishes. In order to be fully specified, seeded iterative jet algorithms must deal with two issues [54]:

1. What are the criteria for seed selection?
2. What should one do when two cones from different seeds overlap?

Two different modifications of the IC algorithm were proposed in order to resolve these issues. One of them is the IC algorithm with progressive removal approach (IC-PR). This approach avoids any issues with overlapping cones. However, IC-PR algorithms have a drawback, since they are collinear unsafe. The second is the IC algorithm with the split-merge approach (IC-SM). IC-SM algorithms have however the downside related to the infrared unsafety. Detail description of both algorithms can be found in Ref. [53].

The problem of the infrared and collinear unsafety of cone algorithms was solved only recently by the invention of the *SISCone* jet algorithm, which is a seedless infrared-safe cone jet algorithm. A description of the algorithm can be found in [57].

2.3.2 Sequential recombination algorithms

Sequential recombination algorithms are based on a pQCD picture in which jets result from subsequent parton branchings. Therefore, the principle of sequential recombination algorithms lies in stepwise recombination of two particles, which are close to each other. These algorithms are used for jet reconstruction in hadronic collisions. Among them, the most widely used algorithms belong to the family of generalised longitudinally invariant k_{T} algorithms [58].

Any version of k_{T} algorithm starts with a list of preclusters, which are formed from calorimeter cells, particles, or partons [54]. Further, the algorithm reconstructs jets as follows [59]:

1. For each pair of particles (*i,j*) one defines two sets of distances:
   - *inter-particle distance*
   $$d_{ij} = \min(p_{\mathrm{T}_i}^{2p}, p_{\mathrm{T}_j}^{2p}) \frac{\Delta R_{ij}^2}{R^2}, \tag{2.3}$$
   where min(. . .) means that from the powers of particle transverse momenta $p_{\mathrm{T}_i}^{2p}$ and $p_{\mathrm{T}_j}^{2p}$ one chooses the minimum value, ΔR_{ij} is defined by Eq. (2.2), R is a jet radius and p is a free algorithm parameter;
   - *beam distance*
   $$d_{i\mathrm{B}} = p_{\mathrm{T}_i}^{2p}. \tag{2.4}$$
2. Among all sets of d_{ij} and $d_{i\mathrm{B}}$ find the minimum $d_{\min}$:
   - If $d_{\min}$ is d_{ij}, then particles (*i,j*) are removed from the list and merged into a new particle according to the recombination scheme. The new particle is afterwards returned back to the list;
   - Otherwise, $d_{\min}$ is $d_{i\mathrm{B}}$ and the object i is declared as a final jet and removed from the list.
3. Return to step 1 and repeat until no particles remain.

The reconstruction procedure sometimes includes also a *jet resolution threshold* parameter d_{cut} below which d_{ij} and $d_{i\mathrm{B}}$ are excluded from the cycle. The most common generalised k_{T} algorithms are: k_{T} ($p = 1$), anti-k_{T} ($p = -1$) and Cambridge/Aachen (C/A) ($p = 0$). The main advantage of the generalised k_{T} algorithms is the infrared and collinear safety.

k_{T} algorithm

The k_{T} algorithm at first recombines particles with low-p_{T} that are close to each other in the $(y - \varphi)$ plane. This leads to the algorithm sensitivity to a soft background, like the underlying event or pile-up. The background presence causes the back reaction [60] of the algorithm resulting in the energy and shape alteration of the reconstructed jet. This feature of the k_{T} algorithm is nevertheless utilised in the background estimations.

anti-k_T algorithm

The anti-k_T algorithm starts jet reconstruction with the recombination of high-p_T particles. Soft particles are recombined with hard ones before they cluster among themselves. Thus, the jet will be resilient to a soft background and has a perfect circular shape (see Fig. 2.2), whereas presence of a high-p_T particle inside the distance $R < \Delta R < 2R$ modifies the jet shape [61]. The soft-resilient feature makes the anti-k_T algorithm to be widely utilised in jet analyses.

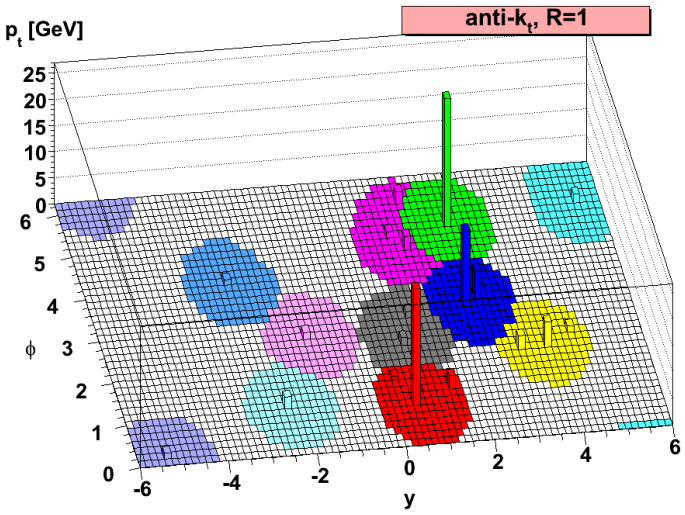

Figure 2.2 – Hard jets reconstructed with the anti-k_T algorithm with $R = 1$. The presence of several high-p_T jets close to each other leads to cone overlaps. Taken from [61].

Cambridge/Aachen algorithm

In the C/A algorithm, the distance estimations become simply geometrical and suffer less from the contamination due to soft backgrounds than the k_T algorithm. The C/A also respects angular ordering of the partonic shower.

2.4 FastJet package

The FastJet package C++ is a powerful software that provides jet reconstruction in p+p and e^-e^+ collisions [50]. FastJet package contains commonly used sequential recombination algorithms such as k_T, anti-k_T and C/A. Cone algorithms can be utilised via special plugins. One of the main benefits of FastJet that it achieves computational time $N\ln N$ for many sequential recombination algorithms instead of N^3, where N is a number of particles in event [50]. Moreover, FastJet includes tools for jet area calculations, background estimation and subtraction.

2.5 Jet quenching

Since jet production is well understood in elementary collisions, jets can be used as a tool to probe the medium produced in ultra-relativistic heavy-ion collisions. Properties of the medium can be then inferred from the observed modifications in jet production. A hard scattering process occurs in the initial stage of the collision, prior to the formation of the QGP. Produced partons propagate through the medium and undergo energy losses. This effect is called *jet quenching* and it was observed for the first time at RHIC [62]. A recent manifestation of the jet quenching in Pb+Pb collisions at $\sqrt{s} = 2.76$ TeV are provided by the CMS experiment [63], see Fig. 2.3. By momentum conservation, the total transverse momentum of the leading jet must

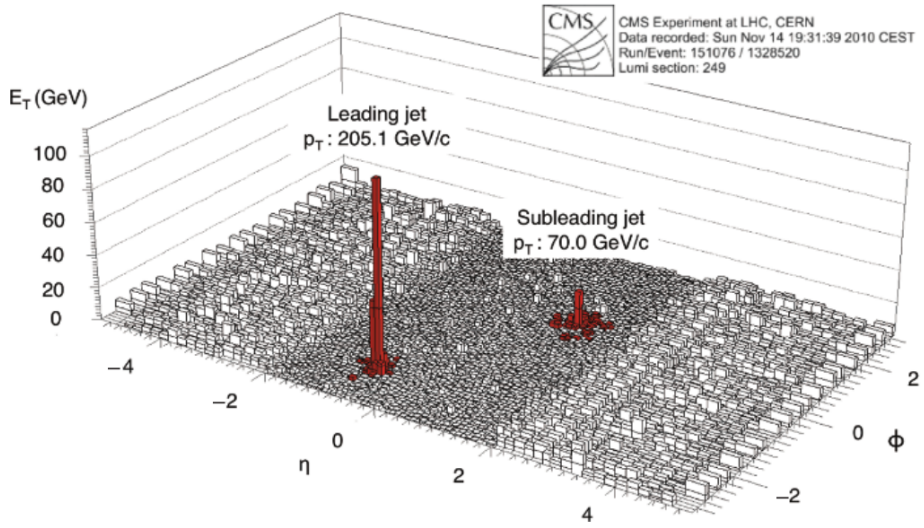

Figure 2.3 – Manifestation of the jet quenching effect in highly imbalanced di-jet events in Pb+Pb collisions at $\sqrt{s} = 2.76$ TeV. The reconstructed jets are labelled with their corrected p_{T}. Taken from [63].

be balanced by recoil jet in the opposite azimuthal hemisphere. Measured subleading jet at $\Delta\varphi \approx \pi$ balances only approximately one third of the momentum of the leading jet. Therefore, recoil parton significantly lost energy by the presence of the medium.

An illustration of the jet quenching effect is shown in Fig. 2.4. On the left part, there is a di-jet production in a p+p collision, where jets are not modified. The energy of the jets is almost the same and they are opposite in the azimuthal angle. The right-hand side plot shows a hard scattering process happening in a heavy-ion collision, where the created medium causes modification of jet properties. Employing p+p collisions as a reference data, it can be seen that the jet quenching effect manifests itself as a yield suppression of the high-p_{T} hadrons and jets. The presence of the QGP influences also the direction of final state jets, since the parent parton experiences a

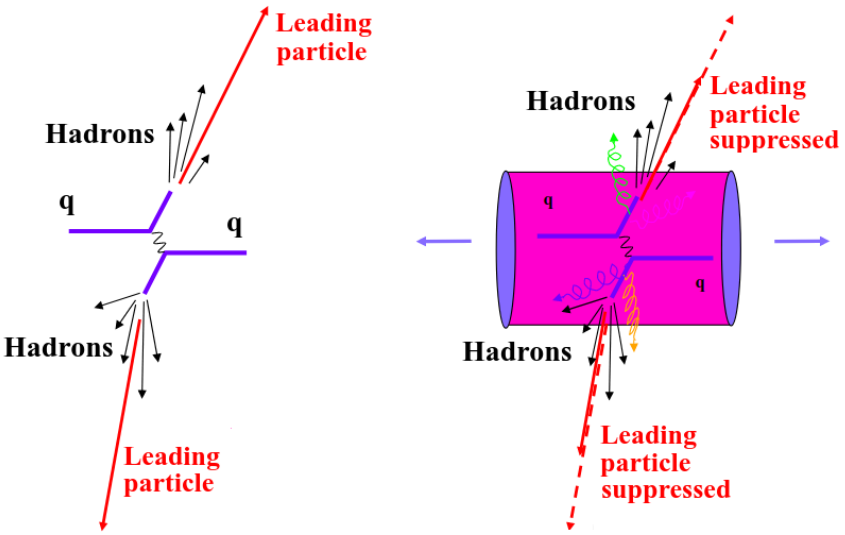

Figure 2.4 – Left: di-jet production in a p+p collision. Right: di-jet production in a heavy-ion collision where jets are modified by the presence of the created QCD medium. Taken from [64].

multiple scattering, that results in the acomplanarity of a di-jet event, i.e. the number of back-to-back jets is suppressed w.r.t. p+p data [65]. Interaction of jet shower with the medium leads also to modification of the internal jet structure [66].

Parton energy losses depend on the medium properties. This fact can be utilised to reveal thermodynamical properties such as particle density and transport properties such as stopping power and transport coefficients [3].

2.6 Background subtraction

Hard scattering processes are rare and in heavy-ion collisions they are accompanied by the intensive, soft, high-multiplicity background, that complicates jet reconstruction. Under these conditions, jet algorithms frequently create also *combinatorial jets* composed of background particles. These particles originate from the *underlying event* (multi-parton interactions, initial and final state radiation) and/or from *pile-up* [67]. For many physics applications, it is crucial to determine the kinematic properties of jets without background contamination.

An experiment independent approach for background subtraction using jet area was proposed in [68]. This method is based on the idea that contamination of hard jets due to the soft background is proportional to a jet area. Reconstructed jet p_{T} is corrected by the expected contribution of the mean underlying event density

employing the following formula:

$$p_{\mathrm{T,jet}}^{\mathrm{reco},i} = p_{\mathrm{T,jet}}^{\mathrm{raw},i} - \rho A^{i}, \tag{2.5}$$

where i runs through all $\mathrm{k_T}$ jets in the event, $p_{\mathrm{T,jet}}^{\mathrm{raw}}$ is a transverse momentum of a jet before correction, A is a jet area and ρ is the underlying event density calculated on event by event basis. The density can be estimated as

$$\rho = \mathrm{median}_{k_\mathrm{T}\ \mathrm{jets}} \left(\frac{p_{\mathrm{T,jet}}^{\mathrm{raw},i}}{A^{i}} \right). \tag{2.6}$$

The average background energy density ρ is calculated as a median of the p_T/A distribution for jets, which are reconstructed by means of the k_T algorithm. The median value is taken in order to exclude true hard jets from the background energy density estimations, see Fig. 2.5. Formula (2.5) does not take into account the effect of the point-to-point background fluctuations which smear the jet p_T spectra [70]. The smearing due to local background fluctuations needs to be corrected later on by means of unfolding.

An average transverse momentum of particles in a hard process is greater than that of background particles. This fact is often utilised to reduce the population of

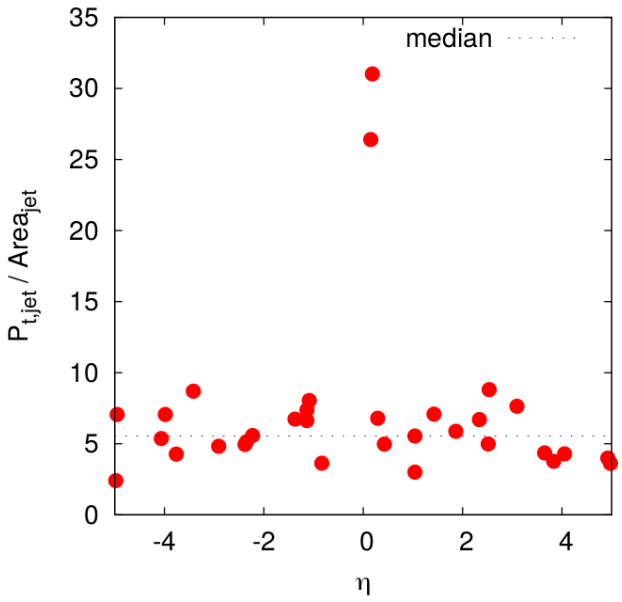

Figure 2.5 – Distribution of p_T/area versus η of jets. The two points that stick out represent hard jets, whereas the other points are combinatorial jets. The dashed line shows the median value of the distribution. Taken from [69].

background particles by introducing a minimum p_{T} cutoff for the jet constituents. However, this method has the downside that the resulting jet sample is collinear unsafe. In addition, background suppression can be performed by requiring to have a high-p_{T} particle inside a reconstructed jet. Such constraint, however, biases the jet fragmentation.

The effect of the underlying events can be also reduced by selecting a smaller jet radius. As noted above, the average number of background particles is proportional to a jet area, which for a conical jet is $A = \pi R^2$. On the other hand, a small jet radius represents a complication for theory predictions, since in this case, one needs to take into account details of the hadronization process [71]. In addition, jets with small radii do not provide an entire picture of the partonic energy loss.

Each experiment, which has published jet measurements in heavy-ion collisions, uses a different approach for jet reconstruction and background subtraction [72, 73, 74]. Further, we will focus our attention on the ALICE experiment. They have elaborated an alternative method of how to suppress combinatorial background jets in the reconstructed jet spectrum which is described in the next section.

2.7 Hadron-jet correlation

Study of jet quenching effect in high-multiplicity environment is a challenging problem due to the presence of a soft uncorrelated background and smearing of the measured p_{T} spectra of true jets by background fluctuations and instrumental effects. It was discussed above, that the number of background jets may be reduced by requiring to have a high-p_{T} particle inside jet candidates. However, such constraint leads to a jet fragmentation bias and breaks down the infrared safety [75]. This bias can affect also selected quenched jets and distort their spectrum. Therefore, another way for reduction of the background jet population without introducing the bias was proposed in work [76]. The method is data-driven and removes the combinatorial background jets by means of statistical subtraction. The method is based on jets that are nearly back-to-back in azimuth w.r.t. a high-p_{T} trigger hadron. Presence of the high-p_{T} particle is clear evidence that a hard scattering has occurred. At the same time, it does not affect fragmentation of the jet in recoil.

2.8 Jet measurements using hadron-jet correlation technique

Figure .2.6 shows a semi-inclusive transverse momentum distribution of jets that recoil from a high-p_{T} hadron (trigger track TT), normalized per one TT, as measured in Pb+Pb collisions at $\sqrt{s_{\mathrm{NN}}} = 2.76$ TeV by ALICE. Azimuthal opening angle enclosed by the trigger hadron and jet was in this case constrained to $\Delta\varphi > \pi - 0.6$. Trigger hadrons were selected from two exclusive p_{T} ranges $(20, 50)$ GeV/c and $(8, 9)$ GeV/c. The signal trigger track ($\mathrm{TT_{Sig}}$), which is from $(20, 50)$ GeV/c, is born on average in hard scattering processes with larger Q^2 than the reference one ($\mathrm{TT_{Ref}}$) which is from $(8, 9)$ GeV/c. For this reason, the associated recoil jets in the

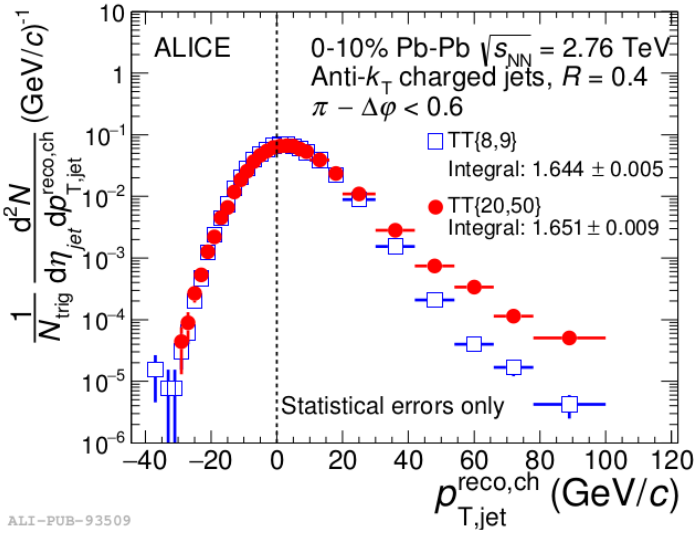

Figure 2.6 – The p_{T} spectra of track-based anti-k_{T} $R = 0.4$ recoil jets associated with two exclusive trigger track p_{T} ranges (20,50) GeV/c and (8,9) GeV/c. Transverse momenta of jets were corrected for average background density on event-by-event basis. Distribution is corrected for the average background energy density. Taken from [65].

first case have a harder p_{T} spectrum than in the latter case. The positive part of both spectra thus shows strong correlation with p_{T} of TT, whereas the negative part, where combinatorial jets dominate, is quite similar for both TT ranges. Further, it is assumed that the number of combinatorial background jets per trigger track is the same for both spectra. If the spectra are subtracted from one another, the contribution of the combinatorial background jets is removed. The subtracted spectrum is called Δ_{recoil} [76] and can be obtained with the following formula:

$$\Delta_{\mathrm{recoil}} = \frac{1}{N_{\mathrm{trig}}} \frac{\mathrm{d}N_{\mathrm{jets}}}{\mathrm{d}p_{\mathrm{T,\,jet}}}\bigg|_{\mathrm{TT_{Sig}}} - C_{\mathrm{ref}} \cdot \frac{1}{N_{\mathrm{trig}}} \frac{\mathrm{d}N_{\mathrm{jets}}}{\mathrm{d}p_{\mathrm{T,\,jet}}}\bigg|_{\mathrm{TT_{Ref}}}, \tag{2.7}$$

where N_{trig} is the number of trigger tracks in the chosen range and C_{ref} is a correction (≈ 0.95) that accounts for the difference in the mean number of physical jets, that are associated to $\mathrm{TT}_{\mathrm{Sig}}$ and $\mathrm{TT}_{\mathrm{Ref}}$ in the limited ALICE acceptance [65]. The main feature of this definition is that Δ_{recoil} variable does not impose bias on jet fragmentation.

The equation (2.7) can be extended to measure the azimuthal distribution of jet yield w.r.t. the momentum direction of the trigger particle in order to study the medium-induced acoplonarity [77]:

$$\Delta_{\mathrm{recoil}}(\Delta\varphi) = \frac{1}{N_{\mathrm{trig}}}\frac{\mathrm{d}N_{\mathrm{jets}}}{\mathrm{d}\Delta\varphi}\bigg|_{\mathrm{TT}_{\mathrm{Sig}}\ \&\ p_{\mathrm{T,\,jet}}} - C_{\mathrm{ref}} \cdot \frac{1}{N_{\mathrm{trig}}}\frac{\mathrm{d}N_{\mathrm{jets}}}{\mathrm{d}\Delta\varphi}\bigg|_{\mathrm{TT}_{\mathrm{Ref}}\ \&\ p_{\mathrm{T,\,jet}}}, \tag{2.8}$$

where $\Delta\varphi$ denotes the azimuthal opening angle between TT and jet

$$\Delta\varphi = \varphi_{\mathrm{TT}} - \varphi_{\mathrm{jet}} \tag{2.9}$$

and $p_{\mathrm{T,\,jet}}$ is some chosen jet transverse momentum bin. The resulting $\Delta_{\mathrm{recoil}}(\Delta\varphi)$ distribution is again obtained by subtracting two per trigger normalized recoil jet yields associated to $\mathrm{TT}_{\mathrm{Sig}}$ and $\mathrm{TT}_{\mathrm{Ref}}$ in the given range of jet transverse momentum. Δ_{recoil} removes all uncorrelated background yield including multiple-partonic interactions (MPI), which is essential for precise acoplanarity measurements. Figure 2.7 shows acoplanarity distribution as measured in central Pb+Pb collisions at $\sqrt{s_{\mathrm{NN}}} = 2.76$

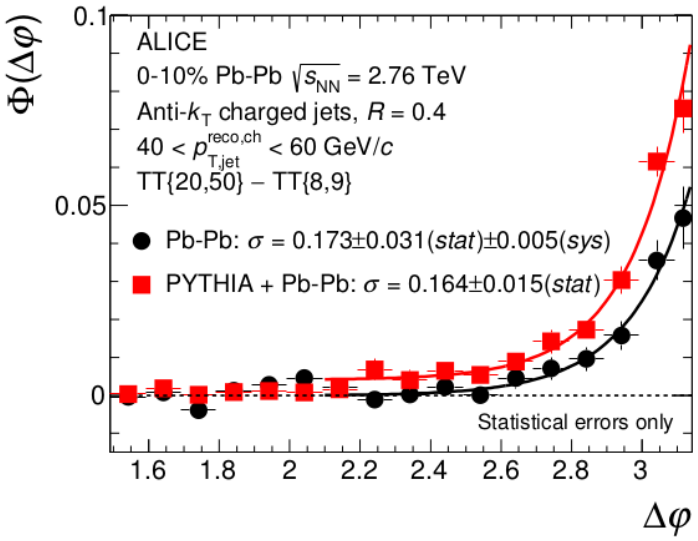

Figure 2.7 – $\Delta_{\mathrm{recoil}}(\Delta\varphi)$ distribution for 0–10 % central Pb+Pb collisions (black markers) and p+p collisions simulated by PYTHIA detector level events embedded into Pb+Pb events (red markers). Parameter σ shows the width of distribution. Taken from [65].

TeV by ALICE. The measured data are compared with acoplanarity distribution ob-

tained by embedding PYTHIA p+p events into real events. Broadening of the peak would be a signature of the medium-induced acoplanarity, whereas enhancement in the tail of the distribution would be a hint for existence of quasi-particle nature of the created QGP, see [65] for more details.

3 A Large Ion Collider Experiment

A **L**arge **I**on **C**ollider **E**xperiment (ALICE) is one of the four big experiments at the LHC. The physics program of the ALICE collaboration is vast [78], but the main focus is on studying properties of the quark-gluon plasma created in ultra-relativistic heavy-ion collisions. Additionally, the ALICE experiment pursues collisions of small systems such as p+p and p+A[1], which are utilised as a reference data for A+A collisions. The detector was designed to be able to provide reliable particle reconstruction and identification in a high-multiplicity environment.

The ALICE detector systems can be divided into three parts: central barrel detectors, forward detectors and the MUON spectrometer (see Fig. 3.1). Detailed information about each part can be found in Ref. [79].

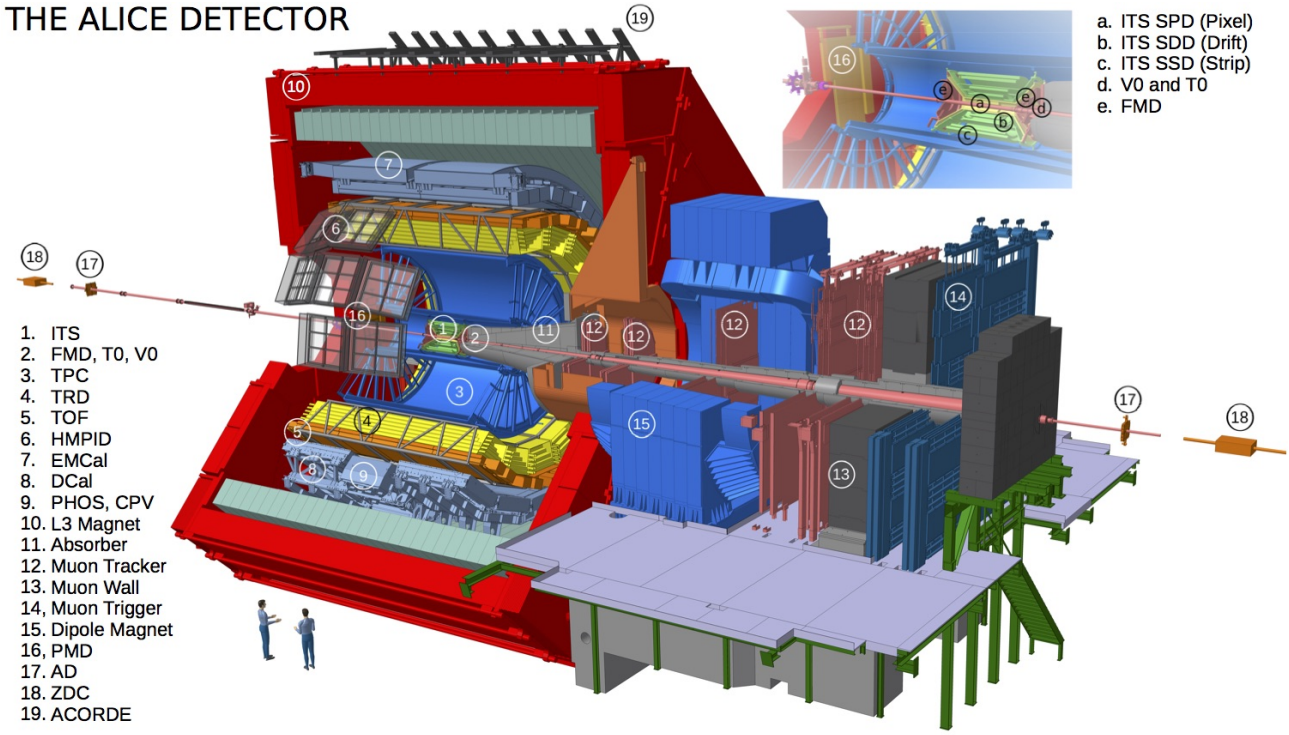

Figure 3.1 – Schematic view of the ALICE detector at the LHC. The upper right corner: enlarged scheme of the ITS and forward detectors. Explanation of some abbreviations can be found in the text. Taken from [80].

3.1 Central barrel detectors

Detectors in the central barrel cover the pseudorapidity range $|\eta| < 0.9$ and they are located in the L3 solenoid magnet that provides a magnetic field of 0.5 T. The main detectors for charged particle tracking are the Inner Tracking System

[1] "A" denotes nucleus.

(ITS) and Time Projection Chamber (TPC). They cover the entire azimuth range and provide tracking with momentum resolution $\Delta p_{\mathrm{T}}/p_{\mathrm{T}}$: 1 % below 10 GeV/$c$ and 5 % at 100 GeV/c for tracks inside the TPC acceptance [74].

3.1.1 Inner tracking system

The ITS [79] is located close to the beam pipe and consists of 6 layers of silicon detectors. The two innermost layers are formed by silicon pixel detectors (SPD), the two intermediate layers by silicon drift detectors (SDD) and two outermost layers by silicon strip detectors (SSD). The main objectives of the ITS are to localise both the primary interaction vertices and secondary particle decay vertices, to identify charged particles with $p_{\mathrm{T}} < 200$ MeV/c and, overall, to improve momentum and angular resolution of particles reconstructed by the TPC [81].

3.1.2 Time projection chamber

The detector construction is based on a field cage. The field cage is divided into two drift regions by the central electrode. The electric field in the drift region is created by the Mylar strips wound around 18 inner and outer supports rods [79]. The TPC is operated at high voltage gradients 400 V/cm, with the voltage of -100 kV at the central cathode, that leads to a maximum drift time of 90 μs. Detailed information about the design features can be found in Ref. [79].

The TPC detector provides the following measurements:

– particle tracking;
– momentum measurements of charged particles;
– preliminary particle identification, by measuring the energy losses $\mathrm{d}E/\mathrm{d}x$.

Principal of the detector can be described as follows. Charged particles propagating through the TPC volume ionise the gas along their path. The ionization density depends on momentum and species of particle. Liberated electrons drift toward the multi-wire proportional chambers at the end of TPC plates, while heavy-ions drift to the central electrode. Signal form the end plates is utilised for determination of space point, where ionization has occurred.

3.2 Forward detectors: V0 arrays

The ALICE forward detectors include the V0 detector which consists of two scintillator arrays, V0A and V0C (or VZERO-A and VZERO-C), that measure charged particles in the pseudorapidity ranges $2.8 < \eta < 5.1$ and $-3.7 < \eta < -1.7$,

respectively [82]. Each array covers the full azimuthal range. The V0 detector is mainly utilised for triggering and for determination of centrality and reaction plane angle in Pb+Pb collisions, as well as for beam-induced background estimations in p+p collisions [82].

V0 arrays are located opposite to each other with respect to the beam interaction point (see Fig. 3.2). Each detector is segmented into 32 channels: 4 axial rings, which

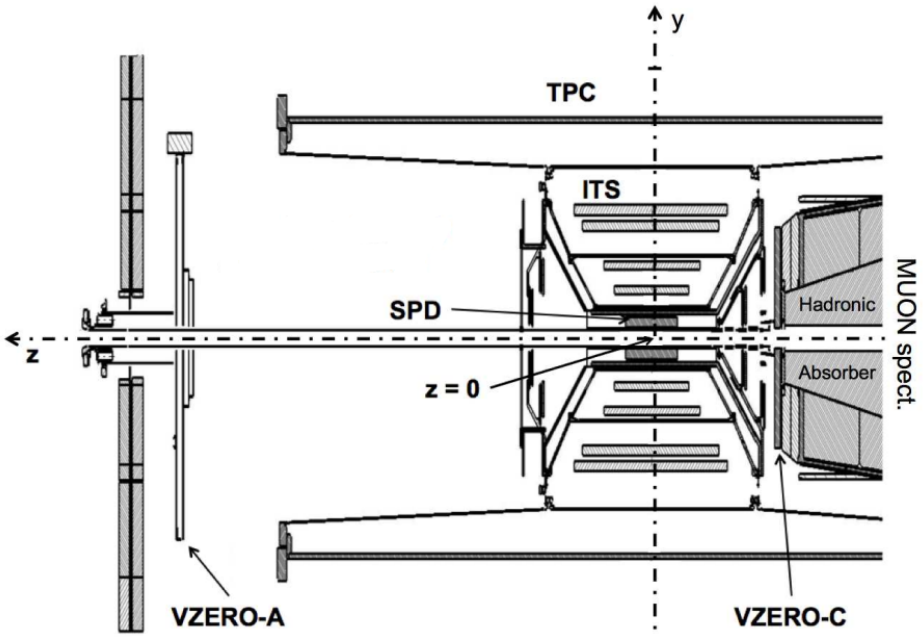

Figure 3.2 – Location of the V0 arrays and of the some detectors, which are quoted in the text. Taken from [82].

are divided into 8 sections. The channels are made of the BC404 plastic scintillator [83] with a thickness of 2.5 and 2.0 cm for V0A and V0C, respectively.

The V0 detector plays a central role in ALICE. It is used to provide minimum bias trigger (coincidence of V0A and V0C) and multiplicity trigger both in p+p and Pb+Pb collisions. A cut on multiplicity measured in V0 biases selected collision geometry. Collisions with a small impact parameter have on average higher V0 multiplicities.

3.3 Muon Arm

The MUON spectrometer is designed to measure the production of heavy-quarkonium states and light vector mesons in the pseudorapidity region $-4.0 < \eta < -2.4$ [80]. It is located at small azimuthal angles $2° - 9°$ in order to provide good acceptance for low-p_T particles [79]. The muon arm starts with a large hadronic absorber, which causes that V0C is positioned closer to the interaction point than V0A.

3.4 Jet reconstruction in ALICE

Jet reconstruction procedure contains three steps: determination of jet candidates, background subtraction and corrections for energy resolution and energy scale [74]. Jet candidates are reconstructed employing the anti-k_{T} algorithm from the FastJet package [50]. The ALICE allows to reconstruct track-based jets as well as full jets. Track-based jets are reconstructed from central barrel charged tracks with $p_{\mathrm{T}} > 0.15$ GeV/c in the pseudorapidity range $|\eta_{\mathrm{track}}| < 0.9$ and full azimuth. Reconstruction of full jets takes into account also energy deposited in electromagnetic calorimeters (EMCal, PHOS, DCal). These calorimeters have however more limited acceptance in pseudorapidity and azimuth. In order to exclude partially reconstructed jets, that appear at a border of acceptance, a fiducial cut on jet pseudorapidity is applied, e.g. for track-based jets in the central barrel it is required $|\eta_{\mathrm{jet}}| < 0.9 - R$.

The background subtraction is performed utilising a modified version of the approach, which was described in Sect. (2.6). Two hardest (leading) reconstructed k_{T}-jets are excluded from the estimation of the median in order to reduce the impact of true jets on the background calculations [84].

Background fluctuations and detector effects smear jet p_{T}. A reconstructed jet p_{T} spectrum thus needs to be corrected for this smearing. The smearing can be described by a response matrix, that gives a probability that a jet with an initial momentum $p^{\mathrm{part}}_{\mathrm{T,\,jet}}$ will be reconstructed as a jet with some $p^{\mathrm{det}}_{\mathrm{T,\,jet}}$ momentum. The relation between the true and the resulting measured spectrum is then assumed to be linear

$$m = W \cdot t, \tag{3.1}$$

where m and t are vectors representing the measured and true spectrum, and W is the response matrix. Since W is often singular, this equation has to be solved by means of unfolding techniques [85, 86, 87].

4 Measurements of hadron-jet acoplanarity in MB and HM p+p collisions at $\sqrt{s}$ = 13 TeV

In 2016 – 2018, the ALICE experiment at the LHC collected a large data sample of p+p collisions at $\sqrt{s}$ = 13 TeV. Data taking was steered with a system of online triggers which allowed for targeted selection of events of interest. Besides the minimum bias trigger, which required a coincidence of V0A and V0C signals, there was also a trigger on rare events which had high particle multiplicity (HM) in the V0 arrays. Light yield collected from V0A and V0C is proportional to the charged particle multiplicity in the V0 arrays. The sum of both yields is denoted as V0M, V0M = V0A+V0C. The HM trigger selected events having more than 5 times greater mean V0M multiplicity than minimum bias events (MB) denoted as ⟨V0M⟩. Such events constitute 0.1 % of the minimum bias cross section, see Fig. 4.1 [6]. The offline

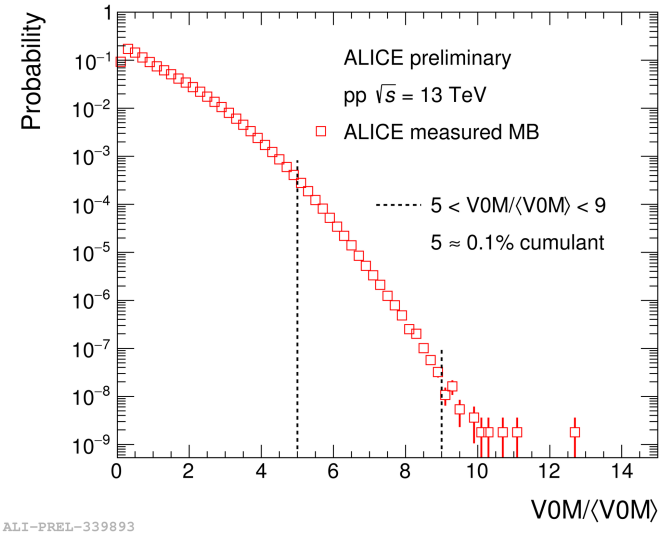

Figure 4.1 – Distribution of V0M/⟨V0M⟩ in minimum bias p+p collision at 13 TeV measured by ALICE. The dashed lines show the range of the applied HM selection. Taken from [6].

selection of HM events required, that HM events have V0M/⟨V0M⟩ constrained also from above to further suppress residual pileup. These HM events were used to search for possible signatures of QGP induced acoplanarity in the h-jet system.

The left part in Fig. 4.2 shows comparison of $\Delta_{\text{recoil}}(\Delta\varphi)|_{p_{\text{T, jet}}}$ distributions for MB and HM p+p collisions at $\sqrt{s}$ = 13 TeV for $\text{TT}_{\text{Sig}}\{20, 30\}$ GeV/c and $\text{TT}_{\text{Ref}}\{6, 7\}$ GeV/c. The selected V0M/⟨V0M⟩ range was 5 – 9. The left panel in Fig. 4.2 shows a remarkable suppression of the back-to-back correlation in the h-jet system for HM triggered events w.r.t. MB events. This could be a sign of the jet quenching effect, but it could be also some detector effect. In order to exclude the

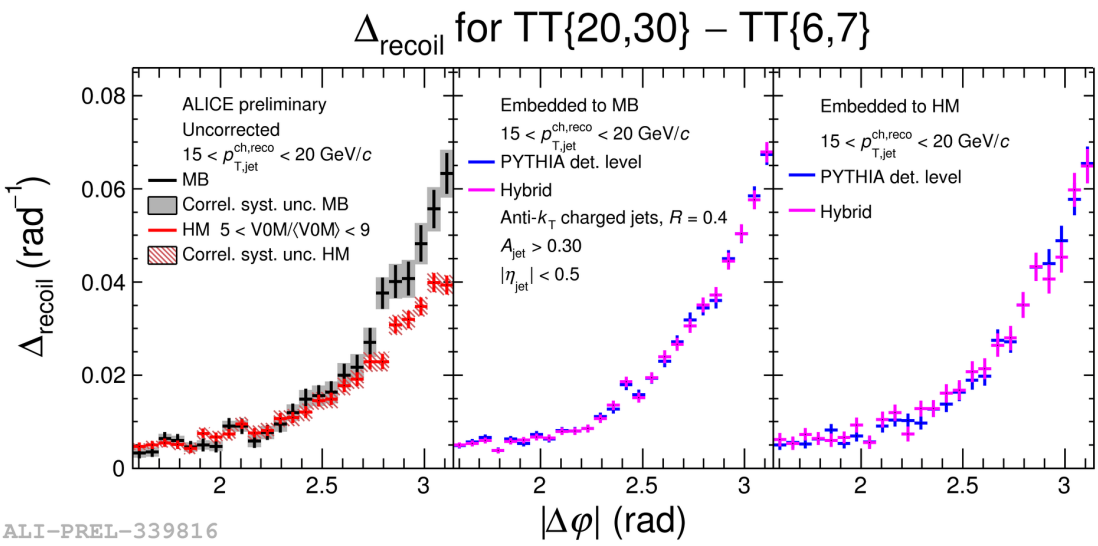

Figure 4.2 – Δ_{recoil} distributions as a function of azimuthal opening angle between TT and a jet in MB and HM p+p collisions at $\sqrt{s}$ = 13 TeV. Left: Real uncorrected data. Middle and Right panels show PYTHIA embedded studies (detector level) for MB and HM events, respectively. Chosen jet p_{T} bin and HM ranges can be found in legend. See text for further details. Taken from [6].

latter case, ALICE took jets simulated by the PYTHIA event generator and embedded them into the real MB and HM events. In the next step, they compared $\Delta_{\text{recoil}}(\Delta\varphi)|_{p_{\text{T, jet}}}$ distributions from the PYTHIA detector level events and from the hybrid data, which result from the analysis of the combined PYTHIA and real data events, see the middle and the right panel in Fig. 4.2. Good match between both approaches suggests that the observed effect is not caused by detector effect.

Hadron-jet acoplanarity was further studied using the PYTHIA 8 event generator. Figure 4.3 shows $\Delta_{\text{recoil}}(\Delta\varphi)|_{p_{\text{T, jet}}}$ distributions for raw ALICE data (left) and

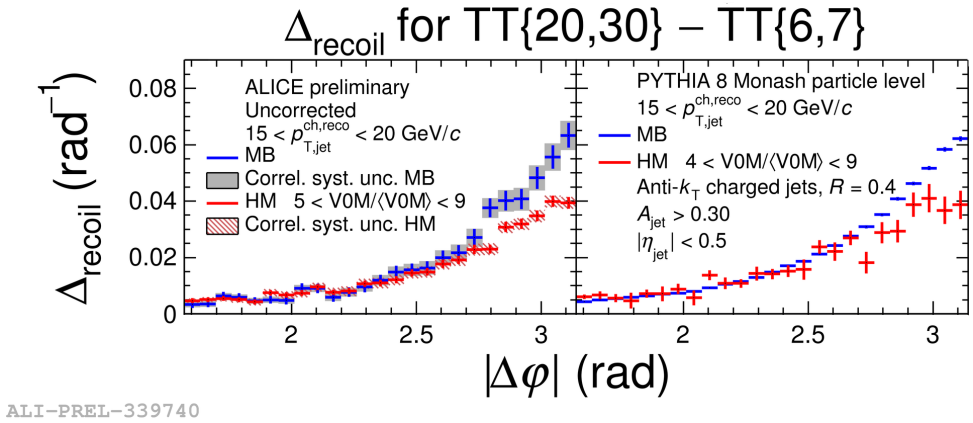

Figure 4.3 – Δ_{recoil} distributions as a function of azimuthal opening angle enclosed by TT and a jet in MB and HM p+p collisions at $\sqrt{s}$ = 13 TeV. Left: Real uncorrected data. Right: PYTHIA particle level simulations. The chosen jet p_{T} bin and HM ranges can be found in legend. See text for further details. Taken from [6].

PYTHIA particle level simulations. The PYTHIA data had relaxed condition on selection of HM events $4 < \mathrm{V0M}/\langle \mathrm{V0M} \rangle < 9$ (right) to improve statistical significance for this qualitative comparison. As can be seen, the PYTHIA simulations exhibit the same suppression feature. This suggests that the suppression is not linked with the jet quenching effect, because the jet quenching effect is not implemented into the PYTHIA generator [7]. Nevertheless, the PYTHIA provides a possibility to search for the origin of this phenomenon. The corresponding analysis is the primary goal of this thesis.

5 PYTHIA 8 simulations

The PYTHIA 8 program [7] is a multi-purpose Monte Carlo event generator for high-energy collisions of elementary particles. It contains libraries of hard and soft processes, as well as parameters of physical models for initial- and final-state parton showers, multi-parton interactions (MPI) and particle decay modes. Hadronization process in the PYTHIA is based on the Lund string fragmentation model [88].

The PYTHIA offers the possibility to efficiently calculate rare processes with large Q^2 transfer, which are studied with hadron-jet analysis. User can restrict the phase space of initial hard scattering using PYTHIA functions "PhaseSpace:pTHatMin" and "PhaseSpace:pTHatMax" [89]. The full simulation can be thus divided into several independent simulations in exclusive p_{T}-hard bins. The corresponding outputs have to be then weighted with formula

$$\omega = \frac{\sigma}{N_{\mathrm{events}}}, \tag{5.1}$$

before combining them together. Here σ is cross section of the given hard bin and N_{events} is the number of generated events.

Since some physical processes such as hadronization and MPI cannot be derived in the framework of pQCD, PYTHIA generator contains adjustable parameters for their model description. In order not to alter each parameter independently, PYTHIA provides a list of tunes, which were tuned based on the experimental data [90]. For our simulations, we took the Monash 2013 tune for p+p collisions. This tune takes into account data obtained at the LHC, as well as data from earlier SPS and the Tevatron measurements. The detail description of the Monash 2013 tune parameters can be found in Ref. [91].

The PYTHIA 8 provides detail information about generated particles, for instance:

- kinematic characteristics such as transverse momentum p_{T}, azimuthal angle φ and pseudorapidity η (see Fig. 5.1);
- particle charge;
- particle status code: positive value for particles from the final state and negative for ones from the intermediate stage.

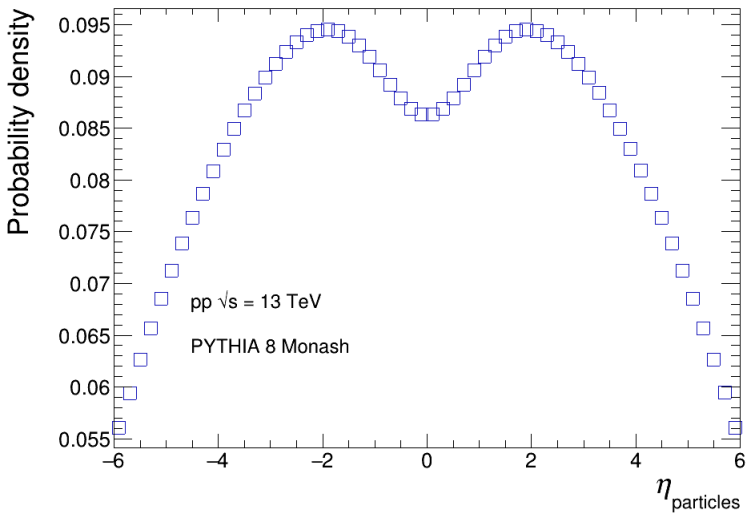

Figure 5.1 – Pseudorapidity distribution of charged final state particles from p+p collisions at $\sqrt{s}$ = 13 TeV simulated by PYTHIA 8 Monash.

Generated charged final state PYTHIA particles are utilised as jet constituents. For jet reconstruction and analysis, we used the FastJet package, see Sect. (2.4). Information about all FastJet's capabilities can be found in Ref. [50].

5.1 PYTHIA 8 settings

Generation of events was performed utilising the following PYTHIA settings:

- the Monash 2013 tune (tune 14);
- beam parameters: p+p collisions at $\sqrt{s}$ = 13 TeV;
- all hard QCD processes ("HardQCD:all = on");
- 21 p_{T}-hard bins (HB) ranging from 3 to 1000 GeV/c;
- independent random seed to avoid statistical dependence of the generated events;
- switching off weak decays of $\mathrm{K}^0_{\mathrm{S}}$, Λ^0, Σ^-, Σ^0, Σ^+, Ξ^-, Ξ^+, Ω^-.

5.2 Processing of PYTHIA events

Detail information about generated events I stored in the output ROOT TTree objects [92]. These objects could have been reprocessed later on to investigate various dependencies between the stored characteristics. I wrote also a ROOT based macros for TTree processing and histogram plotting. For the analysis, I took only events, which contain at least one TT candidate. TT candidates were defined as charged, final state particles from the central barrel $|\eta| < 0.9$ with $p_{\mathrm{T}} \in (20, 30)$ GeV/c ($\mathrm{TT}_{\mathrm{sig}}$) and $p_{\mathrm{T}} \in (6, 7)$ GeV/c ($\mathrm{TT}_{\mathrm{ref}}$). Figure 5.2 illustrates rapid decrease of probability

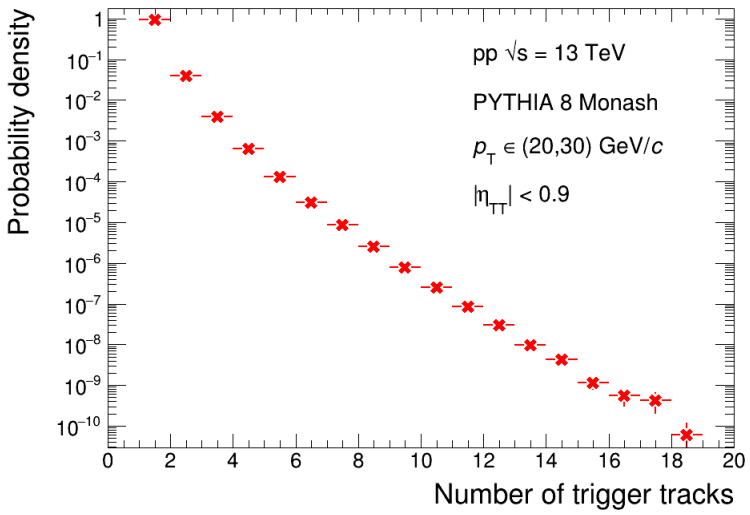

Figure 5.2 – Probability density distribution of the number of TT$\{20, 30\}$ in event.

to have one or more TT$\{20, 30\}$ candidates in an event. In rare cases of several TT candidates, one of them was chosen by random. For such events, I stored:

- V0A and V0C multiplicity determined as the number of charged, final state particles in V0A and V0C detector acceptances (see Sect. (3.2));
- track-based anti-k_T $R = 0.4$ jets reconstructed from final state, charged particles in the central barrel acceptance $|\eta| < 0.9$ with $p_T > 0.15$ GeV/c. Jet centroid axis was restricted to be in a narrower pseudorapidity range $|\eta_{jet}| < 0.5$ such that the reconstructed jet is fully contained in the central barrel acceptance. The similar selection was applied also for the corresponding real data analysis [6];
- charged anti-k_T $R = 0.4$ jets in a wide pseudorapidity range $|\eta_{jet}| < 5.6$, which were reconstructed from final state, charged tracks with $p_T > 0.15\,\mathrm{GeV}/c$ and $|\eta_{particle}| < 6$. Note that the wide pseudorapidity range covers both V0 arrays.

The h-jet analysis is based on the semi-inclusive differential distribution of track-based jets recoiling from a high-p_T TT. The number of recoil jets normalised by the number of TT is equivalent to the ratio of inclusive production cross sections [93]

$$\frac{1}{N_{trig}} \frac{d^2 N_{jet}}{dp_{T,jet}^{ch} d\eta_{jet}}\bigg|_{p_{T,jet} \in TT} = \frac{1}{\sigma^{pp \to h+X}} \frac{d^2 \sigma^{pp \to h+X+jet}}{dp_{T,jet}^{ch} d\eta_{jet}}\bigg|_{p_{T,jet} \in TT}, \tag{5.2}$$

where $\sigma^{pp\to h+X}$ is the cross section to produce a hadron within the $p_T \in$ TT interval, $\sigma^{pp\to h+X+jet}/dp^{ch}_{T,\,jet}d\eta_{jet}$ is the differential cross section for coincidence production of a hadron with $p_T \in$ TT and a track-based recoil jet with transverse momentum $p_{T,\,jet}$ and pseudorapidity η_{jet}. The requirement of TT presence affects the efficiency of the equality in Eq. 5.2. As shown above, a few percent of events contains more than one TT candidate, where only one is chosen. As a result, not all TT candidates make a contribution to N_{trig} and also to the measurement of the inclusive hadron cross section $\sigma^{pp\to h+X}$. It can be seen as a difference between TT p_T distribution and inclusive one, see Fig. 5.3. This selection inefficiency is cancelled in the ratio by h-jet coincidence process (second term on the left-hand side of Eq .5.2) [93].

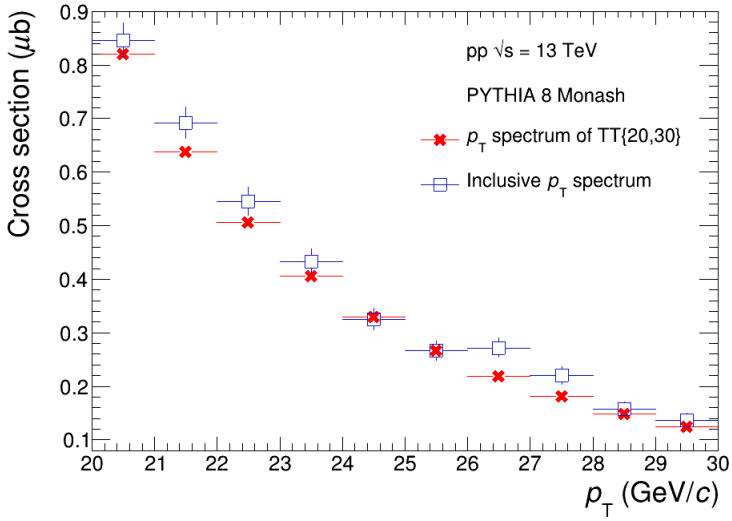

Figure 5.3 – Comparison of p_T spectrum with TT$\{20, 30\}$ requirement and inclusive p_T spectrum.

Jets were reconstructed with the FastJet package using the boost-invariant p_T recombination scheme [50]. Jet p_T was corrected for the mean underlying event density ρ

$$p^{reco}_{T,\,jet} = p_{T,\,jet} - A\rho. \tag{5.3}$$

The underlying event density was found using the technique described in Sect. (3.4). Below, the main results of the simulations will be presented.

5.3 V0 distribution

In this work, V0M multiplicity is defined by summing up charged, final state particles that go to $-3.7 < \eta < -1.7$ and $2.8 < \eta < 5.1$ in the full azimuth. The left-hand side plot in Fig. 5.4 shows a comparison of V0M distributions for true PYTHIA MB events with those events where I required V0A and V0C coincidence

which imitates the minimum bias condition imposed by ALICE. The true PYTHIA

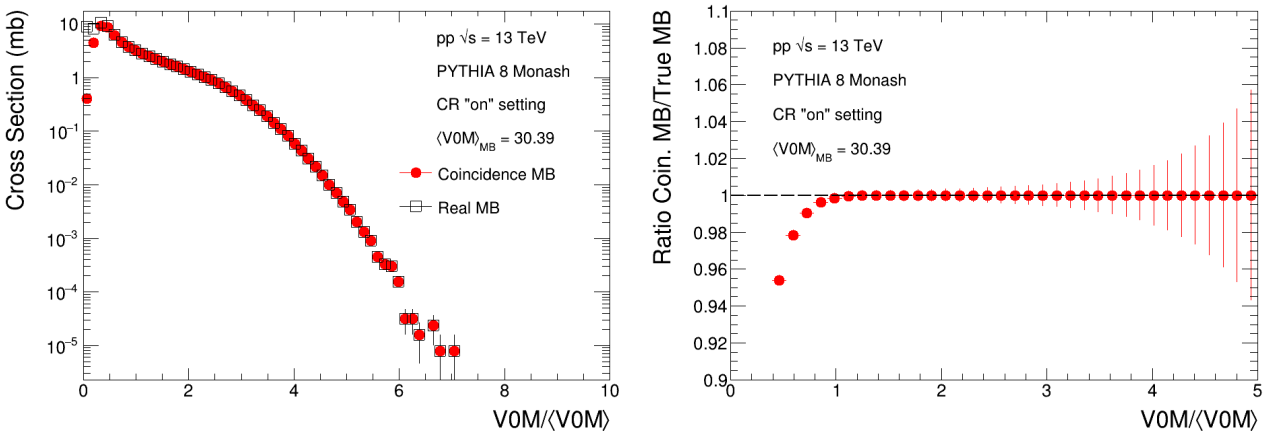

Figure 5.4 – Left: V0M/⟨V0M⟩ distribution in PYTHIA MB events with and without V0A-V0C coincidence. Right: Ratio of the V0M/⟨V0M⟩ distributions from left-hand side figure.

MB events were generated using Soft inelastic QCD processes ("SoftQCD: inelastic = on"). The true MB distribution was obtained without the condition on V0A–V0C coincidence. Both distributions have identical shape above V0M/⟨V0M⟩ > 1, see the right panel in Fig. 5.4. For normalisation of V0M signal, I used the mean value of the coincidence V0M distribution $\langle \mathrm{V0M} \rangle_{\mathrm{MB}} = 30.396$, similarly as it was done in the experiment. The true PYTHIA MB events have ⟨V0M⟩ slightly lower 25.42. The coincidence condition suppresses low multiplicity processes such as single diffractive events.

In the next step, I studied how the presence of a TT in PYTHIA MB events alters the shape of V0M/⟨V0M⟩ distribution and how V0M/⟨V0M⟩ distributions look like for events with TT{20, 30} and TT{6, 7}. Figure 5.5 illustrates the V0M/⟨V0M⟩ distribution for true MB events and for events with the additional requirement on TT presence. It can be seen, that the TT requirement substantially decreases cross section of such events, especially for the higher p_{T} range. As can be seen, the TT requirement modifies V0M/⟨V0M⟩ shape and leads to increased ⟨V0M⟩, $\langle \mathrm{V0M} \rangle_{\mathrm{TT\{20,30\}}} = 62.52$ and $\langle \mathrm{V0M} \rangle_{\mathrm{TT\{6,7\}}} = 61.98$. The TT requirement selects events with large Q^2 transfer. Such events have on average larger particle multiplicity due to jet production.

The PYTHIA hard bin mode cuts away part of the phase space at low Q^2 and introduces a bias, which is not present in reality. Figure 5.6 illustrates a comparison of the V0M/⟨V0M⟩ distribution in PYTHIA MB data and PYTHIA HB data. In the latter case the lowest p_{T} hard bin starts at 3 GeV/c, therefore HB distribution

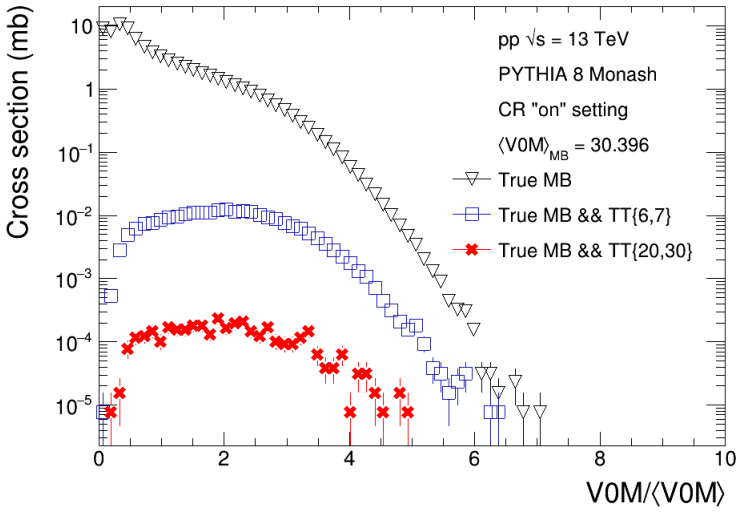

Figure 5.5 – V0M distribution in generated PYTHIA MB events (black triangles). The other two distributions show V0M/⟨V0M⟩ for MB events with TT condition.

differs form MB. However, the same distributions with TT requirement exhibit only minor differences, see Fig. 5.6. Hadron-jet correlation analysis, where we require the presence of a high-p_{T} TT in events, will thus not be distorted by constrained phase space due to hard bins mode.

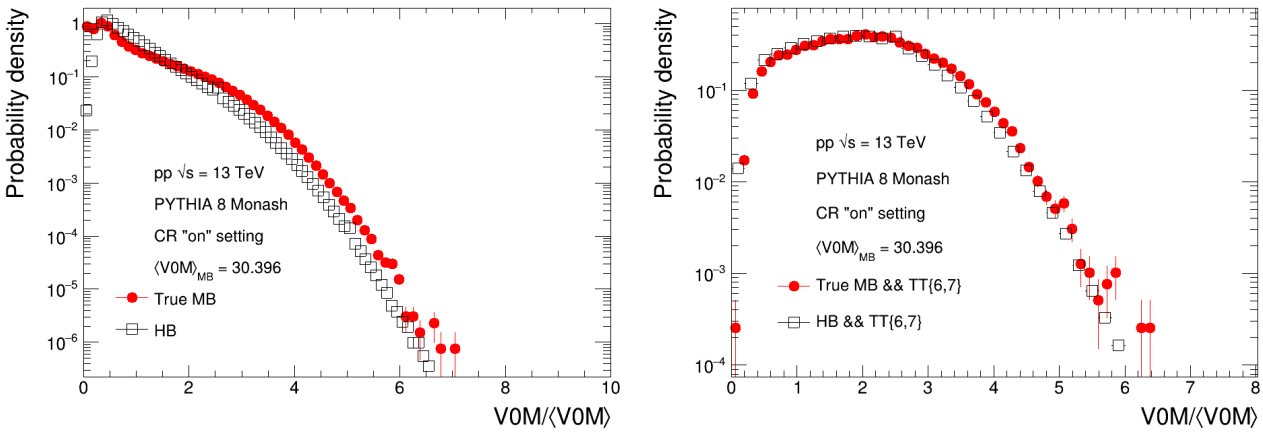

Figure 5.6 – V0M/⟨V0M⟩ distribution generated with PYTHIA true MB mode ("SoftQCD: inelastic = on") and using the PYTHIA hard bin mode. Left: presence of TT was not required. Right: with TT presence.

The left panel in Fig. 5.7 compares the shapes of V0M/⟨V0M⟩ distributions for events with different TT requirements. It can be seen, that different TT biases result in a similar multiplicity V0M. In larger collision systems, such as p+Pb or Pb+Pb, this behaviour is a signal that different TT requirements select similar geometry bias [93].

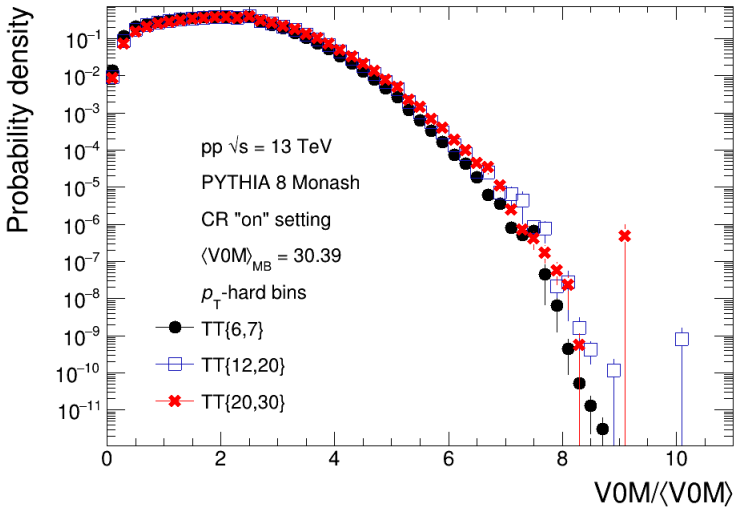

Figure 5.7 – Comparison of V0M/⟨V0M⟩ distributions for events with different TT requirement.

The PYTHIA allows for turning off and on different parts of collision process such as initial- and final-state radiation (ISR and FSR), MPI and colour string reconnection (CR) [94]. I have further studied the effect of these settings on the resulting V0M distributions. Initial- and final-state radiation are related to gluon emission by incoming and outgoing partons, respectively. MPI gives PYTHIA a possibility to have multiple hard processes happening in one collision. The outgoing partons are then interconnected with colour strings, which stretch and hadronize. The colour reconnection switch tells to PYTHIA whether the topology of these colour strings should be optimized in terms of potential energy. Figure 5.8 presents V0M/$\langle$V0M$\rangle_{\mathrm{MB}}$ distributions calculated when PYTHIA flags ISR, FSR, MPI and CR are switched off, see the legend. The obtained mean values ⟨V0M⟩ for each distribution are presented in Table 5.1. It can be seen, that MPI, initial- and final-state radiation processes must be taken into account to reach the expected span of V0M/⟨V0M⟩ distribution seen in the experiment (Fig. 4.1). CR "off" case does not reconnect partons from different

Table 5.1 – ⟨V0M⟩ values obtained when different parts of PYTHIA events were switched off

	All "on"	ISR "off"	FSR "off"	MPI "off"	CR "off"
⟨V0M⟩	30.39	21.22	26.62	13.37	40.64

MPI processes, which leads to a greater number of produced particles.

Figure 5.9 presents a comparison of V0M/⟨V0M⟩ distributions obtained from PYTHIA events with TT$\{20, 30\}$ requirement for CR modes "on" and "off". In the

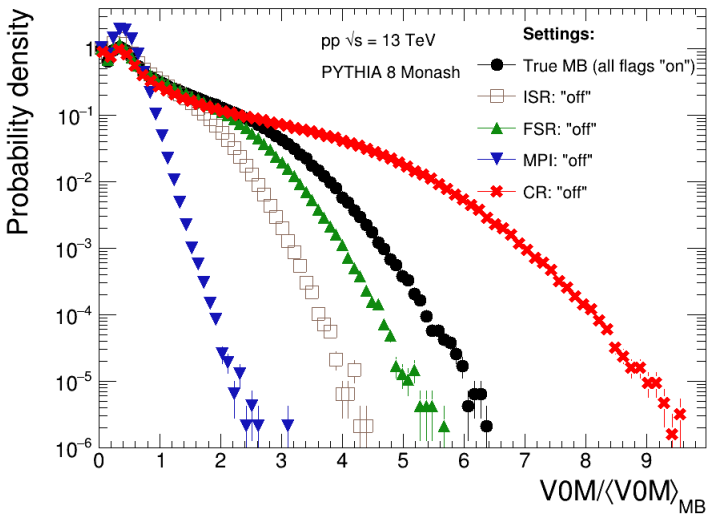

Figure 5.8 – V0M/⟨V0M⟩ distribution as generated by PYTHIA 8 Monash when switching off different parts of PYTHIA event. Presence of TT was not required.

case of CR "off" flag, V0M/⟨V0M⟩ distribution was normalised by the mean value ⟨V0M⟩ from PYTHIA MB events, see Tab. 5.1. It can be seen, that the two CR modes result in qualitatively similar shape of V0M/⟨V0M⟩. Nevertheless, when CR flag is switched off, smaller number of MPI is needed on average to achieve given V0M.

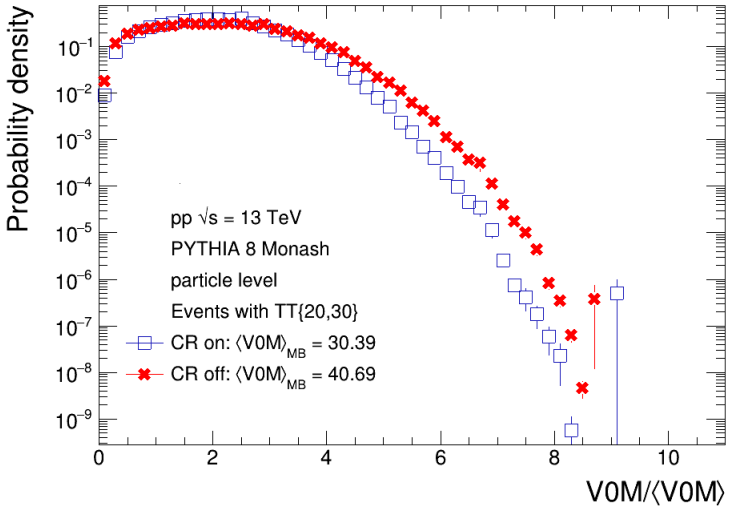

Figure 5.9 – Comparison of V0M/⟨V0M⟩ distributions from PYTHIA HB events with TT{20, 30} condition for CR "on" and "off" modes.

5.4 Semi-inclusive recoil jet distribution

In this section, I will show per trigger normalised recoil jet yields corresponding to different CR modes. When the CR is "on", outputs of different MPI are not independent, since PYTHIA optimises topology of colour strings by making interconnections. These interconnections then affect also resulting jets. One of the questions,

that was raised by the PYTHIA team when ALICE presented the p+p h-jet measurements at the Quark Matter 2019 conference [6] was whether the observed suppression pattern depends on the CR scheme. Therefore, I have simulated PYTHIA events with CR flags "off" and "on", and compared $\Delta_{\text{recoil}}(\Delta\varphi)$ for both settings.

Figure 5.10 presents per trigger normalised recoil jet yields associated to TT{20, 30} and TT{6, 7} for MB and HM events with different CR flags. Transverse

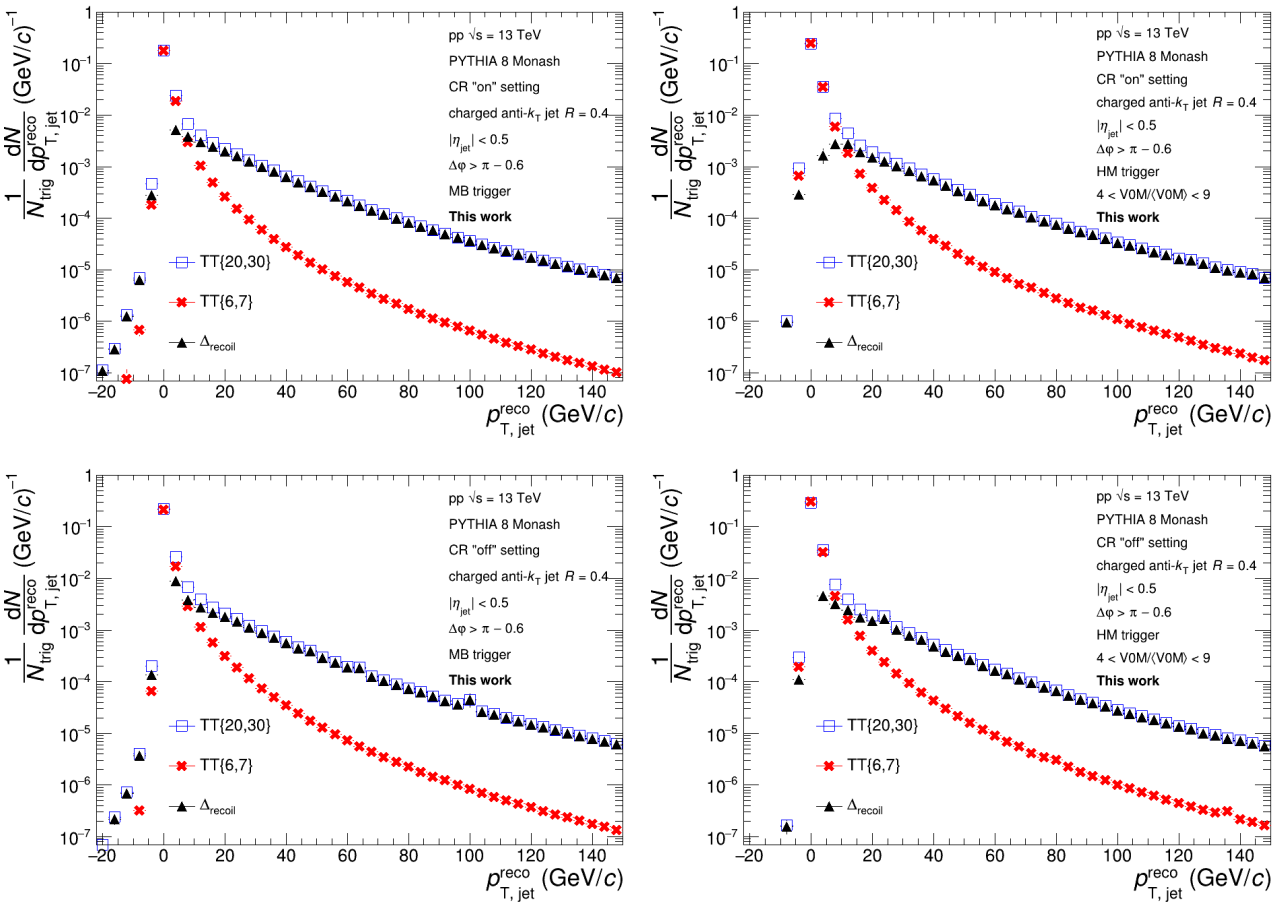

Figure 5.10 – Per trigger normalised recoil jet yields associated to TT{20, 30} and TT{6, 7} for MB (left) and HM (right) events generated with PYTHIA 8 Monash. The corresponding Δ_{recoil} distribution is also shown. Data for CR "on" (top) and "off" (bottom) settings are presented separately.

momentum of jets was corrected for the mean underlying event density ρ using formula (2.6). The reference normalisation factor C_{ref} was calculated as a ratio of the per trigger normalised recoil jet yields associated to TT{20, 30} and TT{6, 7} in the $p_{\text{T, jet}}^{\text{reco}}$ bin 0 – 1 GeV/c. C_{ref} values can be found in Tab. 5.2. Δ_{recoil} distributions were obtained from (2.7).

Figure 5.11 shows comparison of Δ_{recoil} distributions for MB and HM events obtained with different CR modes plotted on top of each other. We can see, that the suppression of HM events w.r.t. MB can be already seen in these plots, which indicate

Table 5.2 – Values of the C_{ref} factor for MB and HM events with different CR flags

	MB events	HM events
CR “on” data	0.983	0.962
CR “off” data	1.008	0.996

that the suppression grows as jet $p_{\text{T, jet}}^{\text{reco}}$ decreases. Data with CR “off” exhibit the same effect, but with lower amplitude.

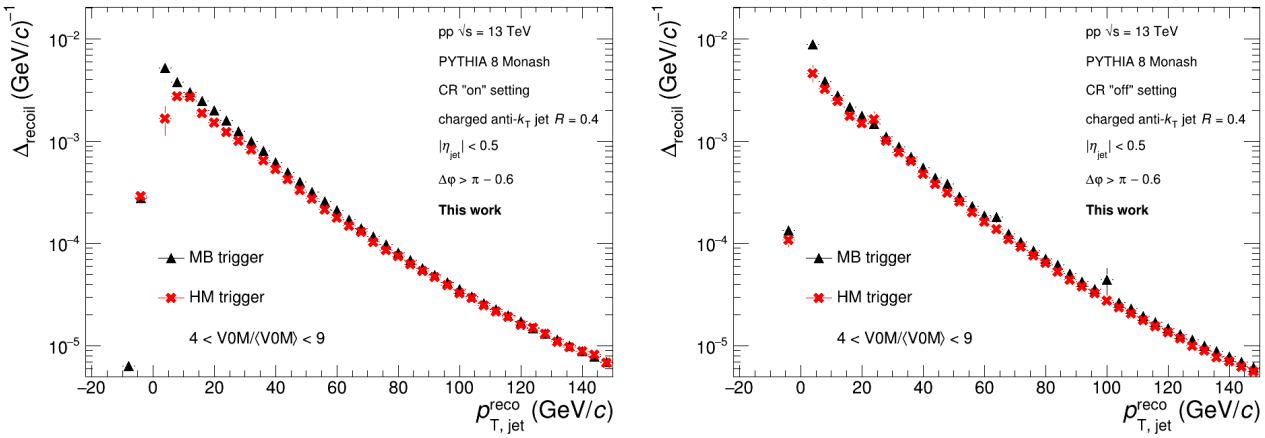

Figure 5.11 – Comparison of Δ_{recoil} distributions in MB and HM events. Left: CR “on”. Right: CR “off”.

5.5 $\Delta_{\text{recoil}}(\Delta\varphi)$ distribution

5.5.1 Central barrel

Figure 5.12 shows simulated per trigger normalised recoil jet yields associated to TT{20, 30} and TT{6, 7} as a function of the azimuthal opening angle $\Delta\varphi$ enclosed by TT and recoil jet in MB and HM events. The corresponding $\Delta_{\text{recoil}}(\Delta\varphi)$ distributions were obtained using the C_{ref} values quoted in Tab. 5.2. All distributions in the considered $\Delta\varphi$ range have a peak at $\Delta\varphi = \pi$, which corresponds to back-to-back correlation of TT and a jet in recoil.

Figure 5.13 illustrates Δ_{recoil} distributions as a function of $\Delta\varphi$ in HM and MB events for different CR modes. It can be seen, that generated PYTHIA events in both modes exhibit qualitatively the same suppression effect seen in Fig. 4.3. To quantify the width of the distribution, the spectra were fitted using the formula [65]:

$$f(\Delta\varphi) = p_1 + p_0 \cdot \exp\left(\frac{\Delta\varphi - \pi}{\sigma}\right), \tag{5.4}$$

where p_0, p_1 and σ are fit parameters. The parameter σ corresponds to the width

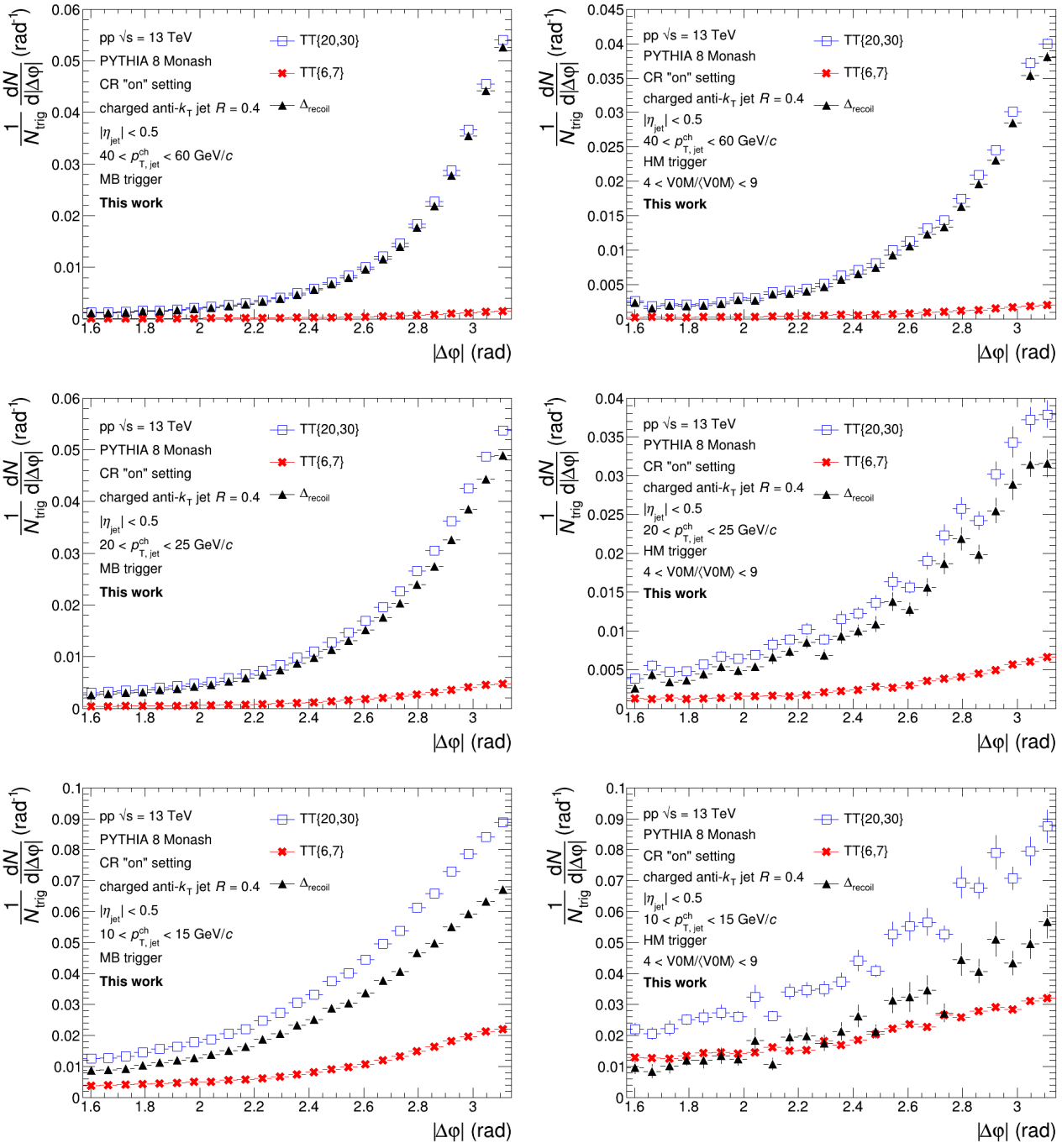

Figure 5.12 – Per trigger normalised recoil jet yields associated to TT{20, 30} and TT{6, 7} in MB and HM events generated by PYTHIA 8 Monash. The panels show also the corresponding $\Delta_{\text{recoil}}(|\Delta\varphi|)$ distributions. Jet $p_{\text{T, jet}}^{\text{ch}}$ range is quoted in legend. CR setting was "on".

of the peak. The obtained σ values are quoted in the legends. It can be seen, that in HM events Δ_{recoil} distributions are broader than in MB. For low jet $p_{\text{T, jet}}^{\text{ch}}$ ranges we see, that statistical precision of the obtained Δ_{recoil} distributions deteriorates. This is due to the fact that in these bins, we get similar per trigger yields of recoil jets for events associated with TT{20, 30} and TT{6, 7}. Therefore, when we are subtracting

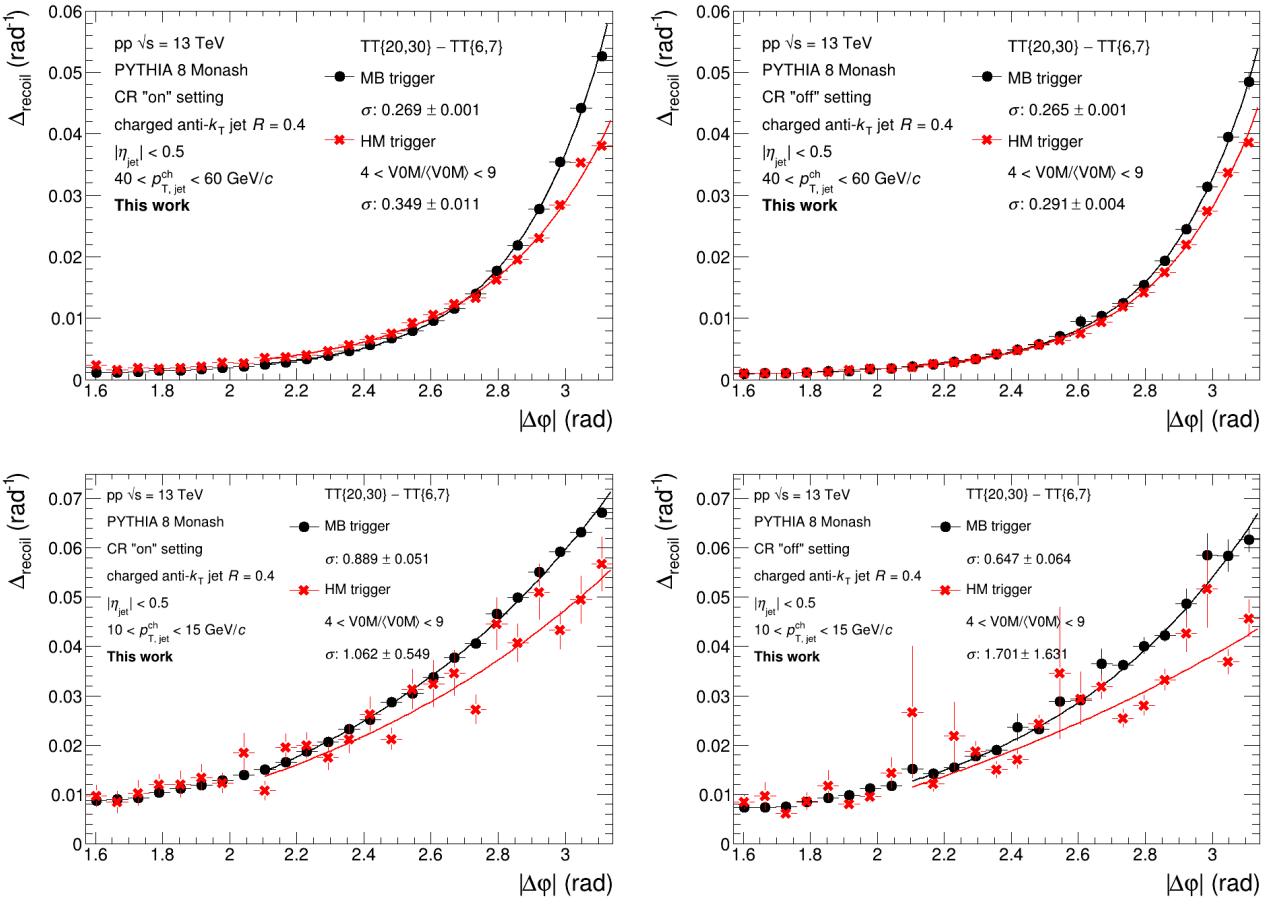

Figure 5.13 – Δ_{recoil} distributions as a function of the azimuthal opening angle between TT and recoil jet reconstructed in the central barrel in MB and HM events for two CR modes: “on” (left column) and “off” (right column). Transverse momentum ranges of selected jets are quoted in legend.

these two close distributions, this results in data points with larger relative errors. In some cases, we see bins with large error bars, where the central value deviates from the main trend, but which have at the same time large statistical uncertainty. These entries emerge from rare events when TT is produced in low-p_T hard bin events. Since these events have a large weighting factor (5.1), they result in data points with a large error bar.

In Fig. 5.14 I directly compared $\Delta_{recoil}(\Delta\varphi)$ distribution for CR “on” and “off” flags in MB and HM events. We see, that both CR modes give quantitatively different results (see legend), but qualitatively they are similar. Therefore, we can conclude, that the observed suppression in HM-acoplanarity distribution is not related to the choice of CR mode and the way how colour strings get interconnected.

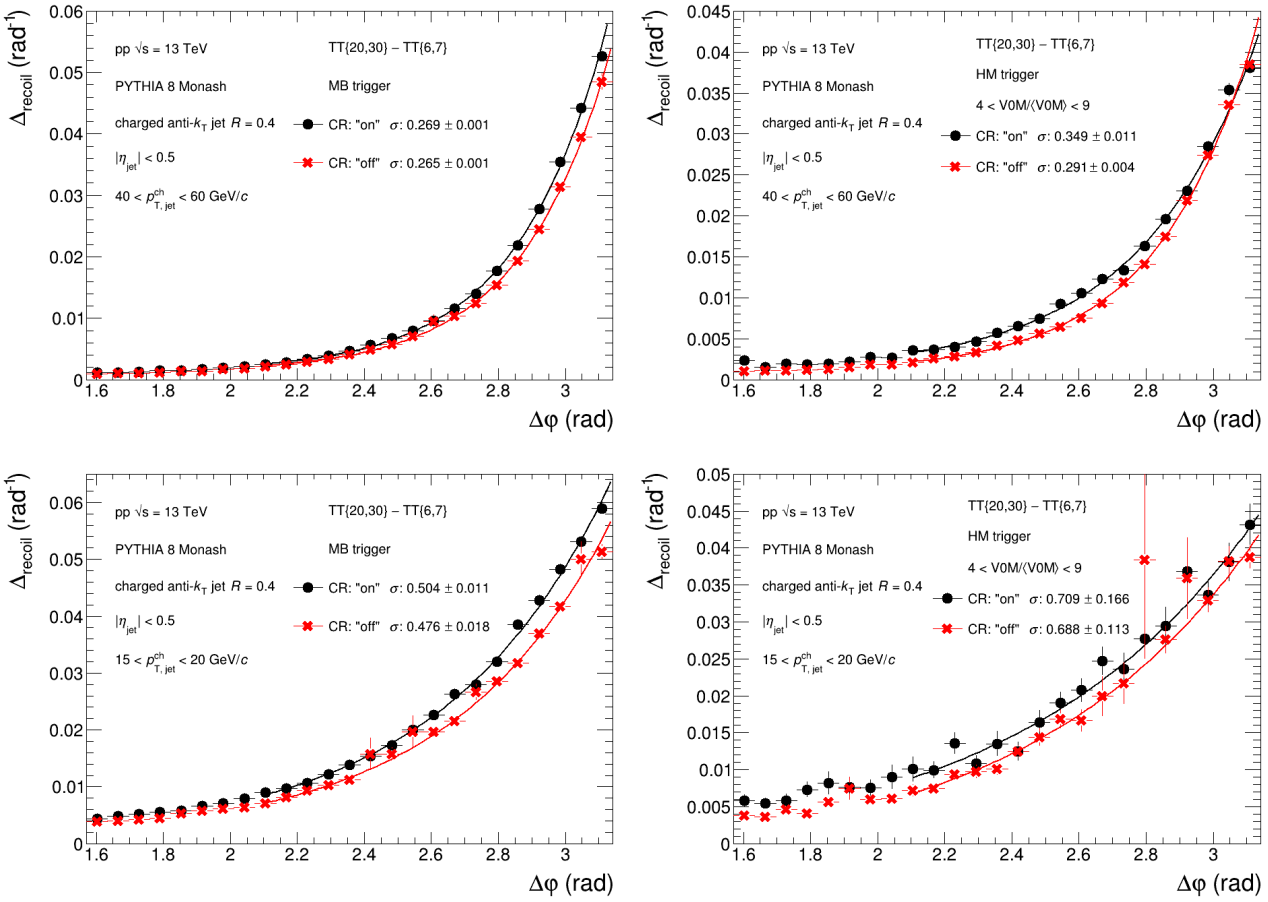

Figure 5.14 – Comparison of Δ_{recoil} distributions for CR modes "on" and "off" in MB and HM events. Transverse momentum ranges of selected jets are quoted in legend.

5.5.2 Wide pseudorapidity range

I have performed the same studies as above also for jets reconstructed in the wide pseudorapidity range $|\eta_{\text{jet}}| < 5.6$, see Fig. 5.15. The motivation for this analysis was to investigate whether much larger pseudorapidity coverage, which is expected to catch a larger fraction of the produced jets, still exhibits the suppression effect. In fact, if this effect would be caused by jet quenching, we should still see the suppression, since lost energy would go away from a jet cone. For simplicity, I chose $C_{\text{ref}} = 1$ for both CR modes, since this factor has only a small effect at high jet p_{T} bins. The distributions were fitted with the function (5.4). In the wide pseudorapidity range, Δ_{recoil} distribution does not exhibit the suppression effect or the magnitude of the suppression is much reduced. However, HM distributions remain to be broader than MB, as can be seen from the obtained σ values (see legend).

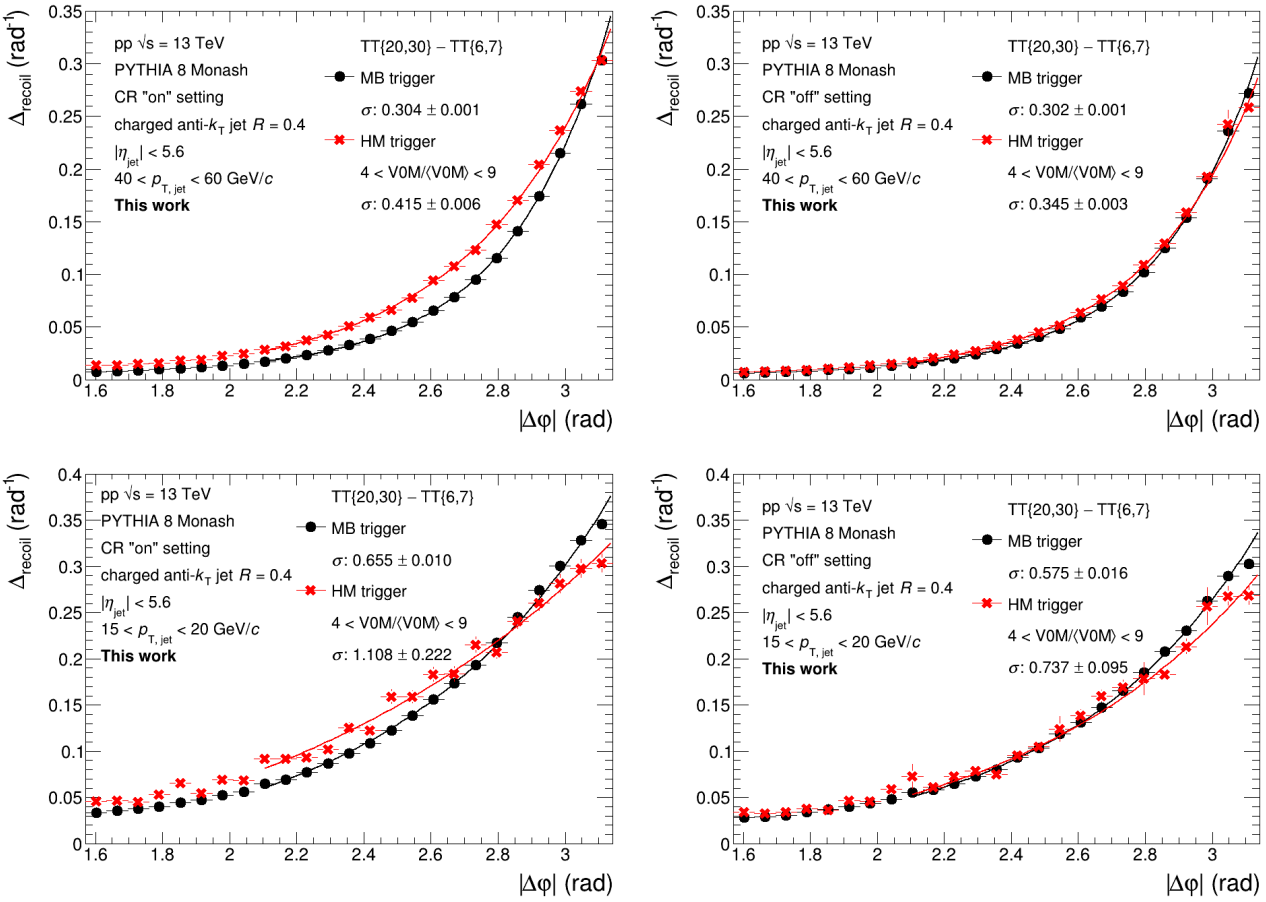

Figure 5.15 – Δ_{recoil} distributions as a function of the azimuthal opening angle between TT and recoil jet reconstructed in the wide pseudorapidity range in MB and HM events for two CR modes: “on” (left column) and “off” (right column). Transverse momentum ranges of selected jets are quoted in legend.

5.6 p_{T}-balance of jets

From the momentum conservation law p_{T} of all jets, generated in a p+p collision, must be balanced. This can be quantified by an asymmetry parameter α

$$\alpha = \frac{\sum_i p^{\text{A}}_{\text{T, jet}_i} - \sum_i p^{\text{B}}_{\text{T, jet}_i}}{\sum_i p^{\text{A}}_{\text{T, jet}_i} + \sum_i p^{\text{B}}_{\text{T, jet}_i}}, \tag{5.5}$$

where $p_{\text{T, jet}}$ is a transverse momentum of a jet. Indices A and B represent an azimuthal hemisphere where a jet is located:

- region A: the same hemisphere as TT (near side region) $|\varphi_{\text{TT}} - \varphi_{\text{jet}}| < \pi/2$;
- region B: the recoil hemisphere $|\varphi_{\text{TT}} - \varphi_{\text{jet}}| > \pi/2$.

Summation goes through all jets p_{T} in a given region.

Figure 5.16 shows distributions of transverse momentum asymmetry for jets with p_{T} above some threshold reconstructed in CB and in the wide pseudorapidity range in MB and HM events with TT$\{20, 30\}$. Obtained distributions for jets with

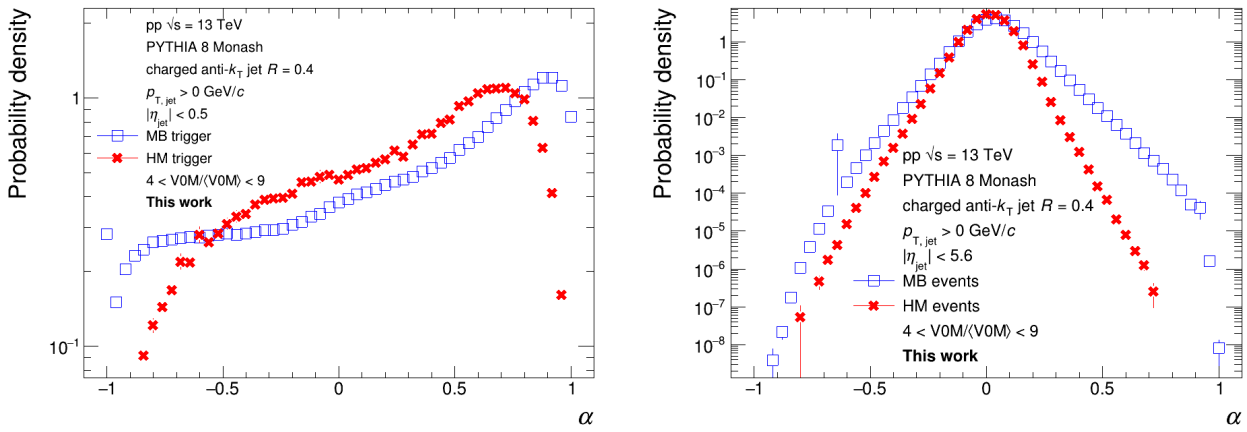

Figure 5.16 – p_{T}-balance distribution of jets with $p_{\mathrm{T}} > 0$ GeV/c reconstructed in CB (left panel) and wide pseudorapidity (right panel) regions in events with TT$\{20, 30\}$ for MB and HM triggers.

$p_{\mathrm{T}} > 0$ GeV/c exhibit a remarkable imbalance for CB region in MB and HM events, whereas for wide pseudorapidity range they are more symmetrical, i.e. they seem to be more balanced. This is telling us that a substantial part of jets event p_{T} is missed in CB. Therefore, we have further studied pseudorapidity distributions of jets in MB и HM events.

5.7 Pseudorapidity distribution of jets

The central barrel acceptance is not big enough, therefore some high-p_{T} jets can be missed. For this reason, I have investigated in PYTHIA η_{jet} distribution of high-p_{T} recoil jets in much broader pseudorapidity interval for MB and HM events with TT. Figure 5.17 illustrates pseudorapidity distributions of recoil jets for MB и HM events with different jet p_{T} cutoff. We see, that while MB events have more or less symmetric distribution, the HM condition enhances probability to find a high-p_{T} recoil jet in the V0C acceptance. The V0A part also exhibits probability enhancement, but it is much lower than in V0C. The asymmetry clearly comes from the asymmetry of the V0 detector, where V0C is by almost 1 pseudorapidity unit closer to mid-rapidity than V0A, see Fig. 3.2. A typical high-p_{T} jet is a shower with a large number of particles. If such a shower hits the V0C array, it may induce the HM trigger to fire. Additionally, I have studied, how different event activity biases in V0M affect the pseudorapidity distribution of recoil jets having $p_{\mathrm{T}} > 25$ GeV/c. The results can be seen in Fig. 5.18,

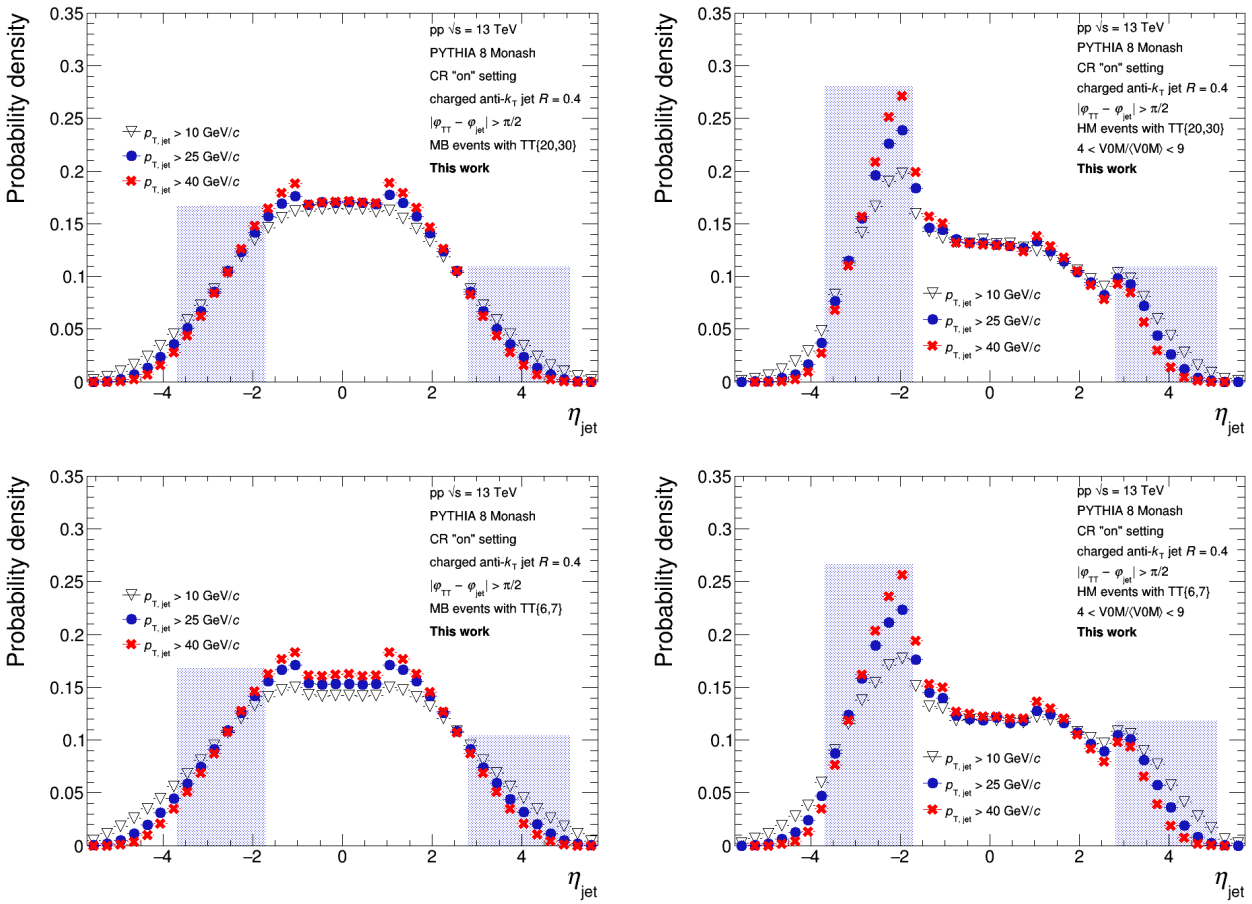

Figure 5.17 – η_{jet} distribution of track-based anti-k_{T} $R = 0.4$ recoil jets for MB (left) and HM (right) events for different jet p_{T} ranges (see legends). Top panels: jet recoling from TT$\{20, 30\}$. Bottom panels: jet recoling from TT$\{6, 7\}$. The blue boxes show V0A and V0C pseudorapidity coverages.

where the probability to find a high-p_{T} recoil jet in the V0 arrays grows with the HM trigger bias.

I have plotted also pseudorapidity distribution of jets in the near side region around TT, see Fig. 5.19. These jets are located in the same azimuthal hemisphere as TT. By construction, there will be always a jet associated with TT in CB. Therefore, the region of CB is enhanced. V0 regions show much less enhancement. Figure 5.20 then shows a direct comparison of the pseudorapidity distributions for the near side and recoil regions. They are normalized per trigger to give the proper relative strength of both spectra.

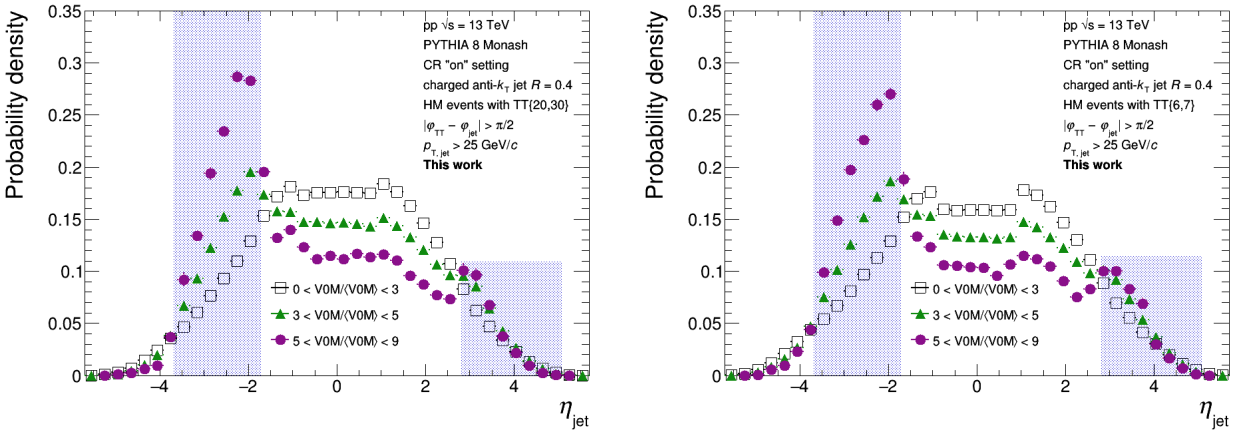

Figure 5.18 – η_{jet} distributions of track-based anti-k_{T} $R = 0.4$ recoil jets with $p_{\mathrm{T}} > 25$ GeV/c for different V0M/⟨V0M⟩ event activity biases in events with TT{20, 30} (left) and TT{6, 7} (right). The blue boxes show V0A and V0C pseudorapidity coverages.

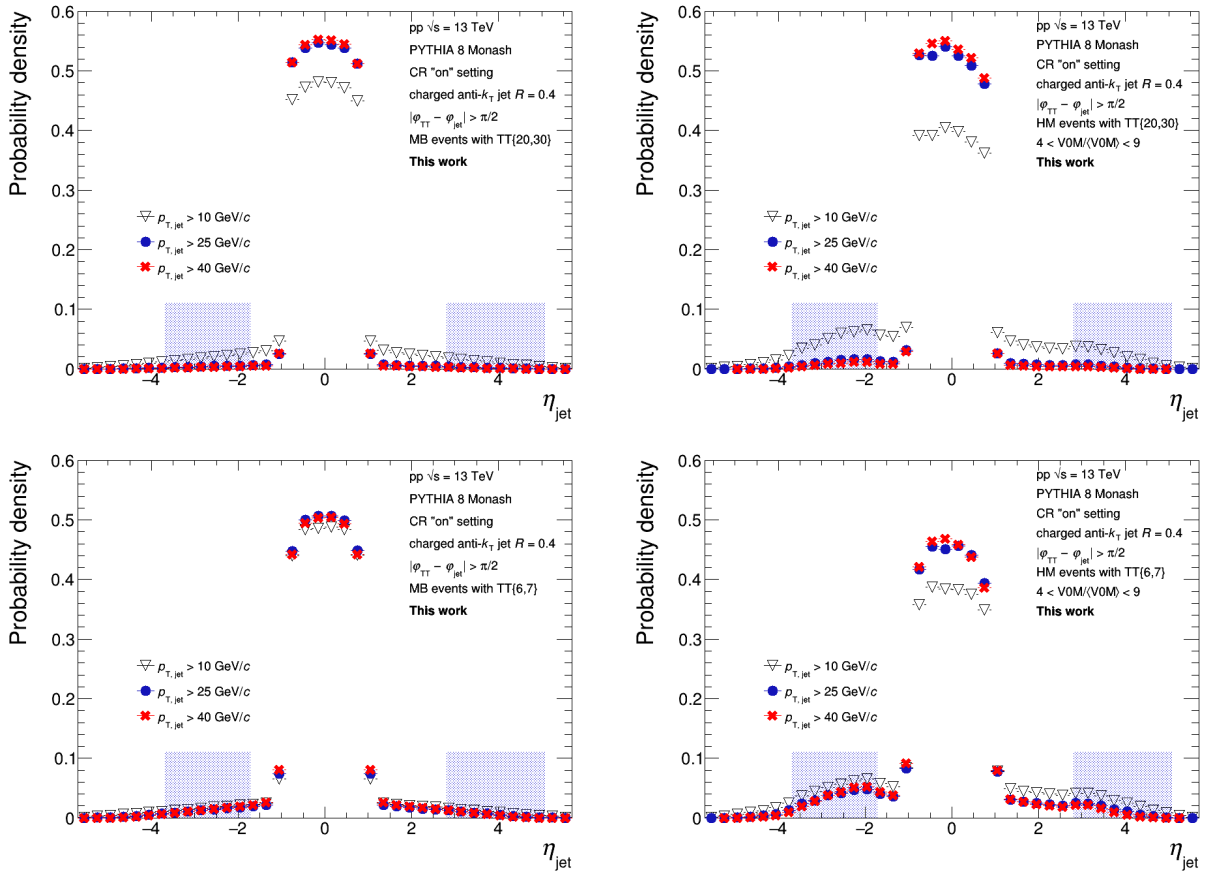

Figure 5.19 – η_{jet} distribution of track-based anti-k_{T} $R = 0.4$ near side jets for MB (left) and HM (right) events for different jet p_{T} ranges (see legends). Top panels: TT{20, 30} hemisphere. Bottom panels: TT{6, 7} hemisphere. The blue boxes show V0A and V0C pseudorapidity coverages.

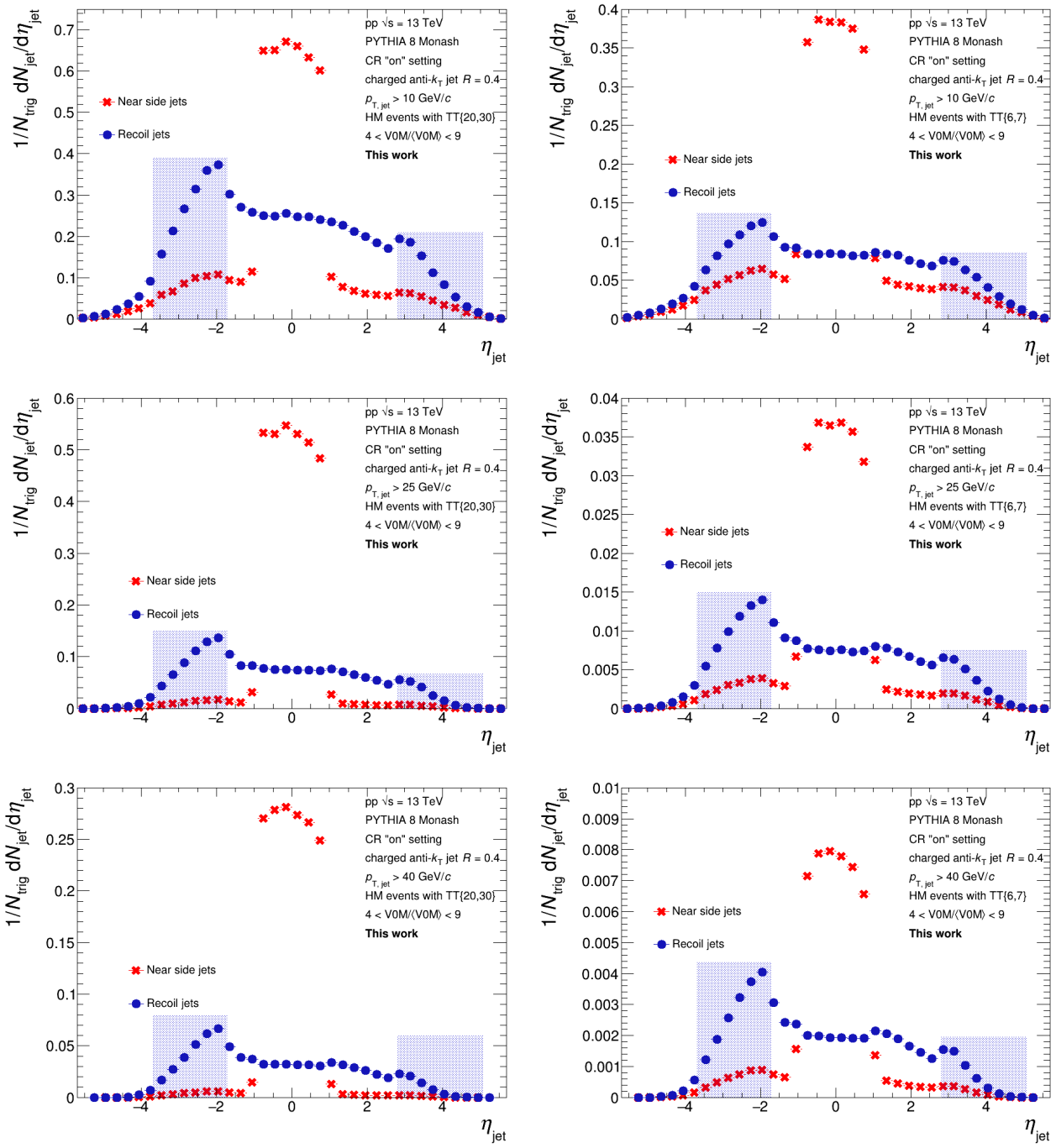

Figure 5.20 – Comparison of pseudorapidity distributions of jets in the near side hemisphere around TT{20, 30} (left) and TT{6, 7} (right) and of jets in the recoil hemisphere. The blue boxes show V0A and V0C pseudorapidity coverages.

5.8 The number of high-p_T recoil jets

5.8.1 Central barrel

Acoplanarity of the measured TT-recoil jet system depends also on the number of jets that are produced in a given event. When there are just two jets in event, they are usually produced back-to-back in azimuth due to momentum conservation. Events

with multiple jets tend to increase acoplanarity. In order to investigate, which kind of jet configurations are suppressed or enhanced with HM condition, I have analysed the distribution of probability to find a given number of recoil jets in an event with p_{T} greater than some threshold, see Fig. 5.21. I considered high-p_{T} recoil jets only in

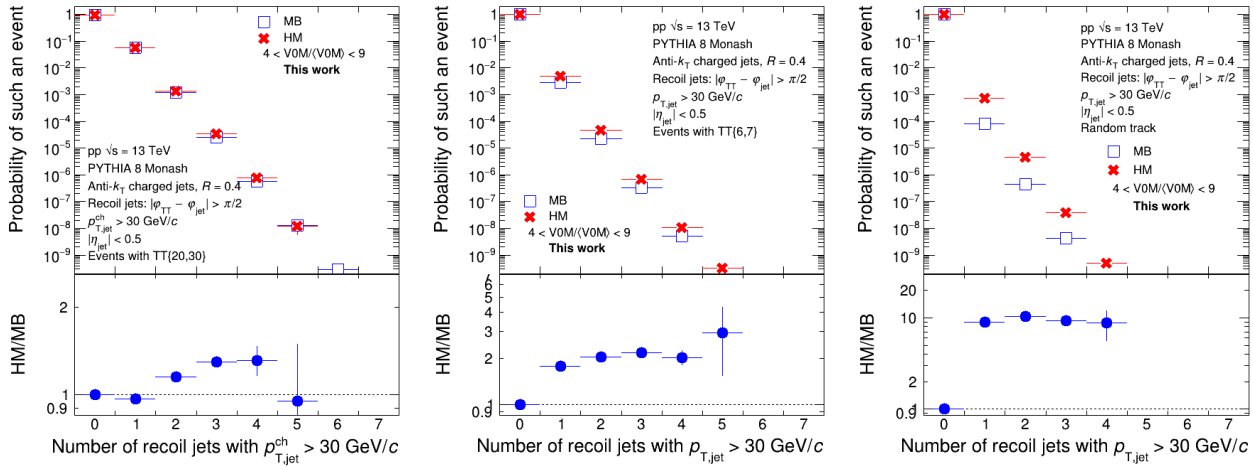

Figure 5.21 – Top panel: Probability to find a given number of recoil jets with $p_{\mathrm{T}} > 30$ GeV/c in MB and HM events with TT{20, 30} (left), TT{6, 7} (middle) and random track (right). Jets were reconstructed in CB region. Bottom panel: HM/MB ratio of the probability density functions.

order to suppress combinatorial background jets. The distributions are steeply falling roughly by an order of magnitude when increasing the number of high-p_{T} recoil jets in event by 1. HM and MB plots have a similar shape, more can be seen from their ratio. There we see, that probability to find a single jet recoiling from TT{20, 30} in CB is suppressed for HM events w.r.t. MB. On the other hand, HM events are likely to have more than one high-p_{T} recoil jet in CB. The missed single recoil jet can induce HM trigger and cause the suppression of the back-to-back correlation in the Δ_{recoil} observable for HM events w.r.t. MB. Enhancement of events with multiple high-p_{T} recoil jets, that we see in HM with TT{20, 30} are not able to compensate for this loss of jet yield, since their probability is much lower. In the case of jets recoiling from TT{6, 7}, we see the opposite behaviour of single jet events. High-p_{T} recoil jet spectrum associated to TT{20, 30} is harder than spectrum associated to TT{6, 7}, therefore we still see the suppression in Δ_{recoil} observable. On average, multi-jet HM events have larger acoplanarity than MB, which is also consistent with the observed broadening of $\Delta_{\mathrm{recoil}}(\Delta\varphi)$ spectra.

To see to what extent can be the presented distributions with TT affected by uncorrelated jets coming e.g. from MPI, I have analysed what is a probability to see

a given number of high-p_{T} recoil jets in a minimum bias event. Here, I assume that each MPI behaves in the first approximation like MB. The results can be seen in the right-hand side of Fig. 5.21. We see a jump roughly by 3 order of magnitude between the probability not to find any high-p_{T} jet and the probability to find a single jet. Thus contamination of uncorrelated high-p_{T} jets is small.

5.8.2 Wide pseudorapidity range

The similar studies were performed for recoil jets in wide pseudorapidity range, see Fig. 5.22. Here we see, that HM condition suppresses the probability of having an event without any high-p_{T} recoil jet.

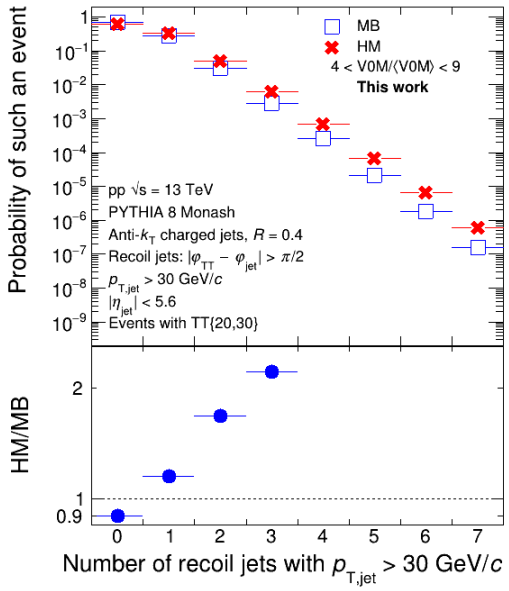

Figure 5.22 – Top panel: Probability to find a given number of recoil jets with $p_{\mathrm{T}} > 30$ GeV/c in MB and HM events with TT$\{20, 30\}$. Jets were reconstructed in the wide pseudorapidity range. Bottom panel: HM/MB ratio of the probability density functions.

Conclusion

Quark-gluon plasma is an exotic state of strongly interacting matter which exists under extreme energy densities and temperatures. It has been predicted nearly 45 years ago by J.C. Collins and M.J. Perry [95] and confirmed by experiments colliding ultra-relativistic heavy-ion beams in 2000. The QGP produced in a laboratory is extremely unstable system with a lifetime of the order of 10^{-23} s and can be therefore investigated using indirect approaches only. The most reliable evidence of the QGP formation is collective particle flow, reflecting the nature of QGP as an ideal liquid, and jet quenching.

The observation of collective flow in collisions of small systems, such as p+Pb and p+p, raised the question concerning the possibility of the QGP formation in such collisions. Therefore, it is necessary to improve the precision of current measurements and to study new observables. In these collision systems, we have so far not seen evidence of the jet quenching. Jet quenching can manifest itself in different ways: suppression of high-p_{T} particle and jet yields, modification of a jet substructure, and deflecting of a jet centroid, which results in acoplanarity.

Jet reconstruction is carried out utilising jet finding algorithms whose main goal is to combine particles and their energy into a final jet. The kinematic characteristics of a final jet are close to those of a parent parton. Since a hard scattering process occurs at the initial stage of a collision, produced partonic showers interact with the medium. This is utilised in the so-called jet tomography of the medium where we use jets as a probe of the created QGP. However, a hard scattering process in heavy-ion collisions is accompanied by intensive underlying events, which represent background for its studies. Advanced analysis tools have to be therefore used to correct measured spectra.

One of the experiments devoted to the investigation of the QGP properties and behaviour is the ALICE experiment at the CERN LHC. During the LHC run 2, ALICE experiment collected p+p collisions data at $\sqrt{s}$ = 13 TeV using two online trigger systems: minimum bias trigger and trigger on rare events, which had high particle multiplicity in the forward V0 arrays. These high multiplicity events were utilised to search for possible signatures of QGP, namely medium-induced acoplanarity in the hadron-jet system [6]. Obtained results showed marked suppression of HM events

w.r.t. MB, which resembles the jet quenching effect. However, qualitatively similar suppression was observed also in events simulated with PYTHIA 8 Monte Carlo generator, which does not account for jet quenching effect. The main goal of the thesis was, therefore, to investigate the origin of the observed phenomenon using the PYTHIA 8 generator.

I have used the PYTHIA 8 generator with Monash tune to simulate p+p collisions at $\sqrt{s}$ = 13 TeV. The generated charged, final state particles were used as jet constituents. Jet reconstruction was performed with anti-k_{T} algorithm $R = 0.4$ in the central barrel and wide pseudorapidity regions. The wide pseudorapidity range covered also the V0 detectors. Transverse momenta of jets in CB were corrected for underlying event density ρ.

Event activity of the analysed events is expressed in terms of V0M/$\langle$V0M$\rangle$, which represents the number of charged particles passing through V0 arrays normalised by its minimum bias value. In the first step, I studied how different parts, that describe the collision process in PYTHIA, affect obtained V0M/$\langle$V0M$\rangle$. It was shown, that in order to obtain the expected span of V0M/$\langle$V0M$\rangle$ distribution seen in the experiment, it is necessary to take into account the multi-partonic interaction, initial- and final-state radiation processes.

Measurements of the acoplanarity are based on hadron-jet correlation technique. This approach analyses jets that recoil from a high-p_{T} hadron in azimuth. The method allows for subtraction of uncorrelated jet yield on ensemble basis using statistical, data driven approach. The background-corrected distribution of opening azimuthal angle in a hadron-jet system is called $\Delta_{\mathrm{recoil}}(\Delta\varphi)$. I have used this observable to quantify acoplanarity in generated data. Obtained HM-acoplanarity distributions in the CB regions exhibit the same suppression effect as the real data. Both colour reconnection modes gave quantitatively different results, but qualitatively they are similar. Due to the momentum conservation law, we expect that p_{T} of all jets in an event must be balanced. Hence, I have analysed p_{T} balance of jets and found, that the CB region exhibits asymmetry, whereas the wide pseudorapidity range is more symmetrical. This signalises that some high-p_{T} recoil jets are missed from CB acceptance. Indeed, obtained $\Delta_{\mathrm{recoil}}(\Delta\varphi)$ distributions in the wide pseudorapidity range do not exhibit the suppression effect or its magnitude is much reduced. Further, I have analysed pseudorapidity distributions of high-p_{T} jets recoiling from TT and found,

that HM events enhance the probability to find a high-p_{T} jet in the V0C acceptance. At the same time, MB events have more or less symmetric shape. It also was shown, that the probability to find a high-p_{T} recoil jet in the V0 arrays grows with the event activity biases in V0M. Obtained pseudorapidity distributions for jets in the near side region around TT exhibit the opposite features: the region of CB is enhanced, since there are always jets associated to TT, and V0 regions show much lower enhancement.

At the final stage of the thesis, I have investigated, which configurations of high-p_{T} recoil jets are suppressed/enhanced by the HM trigger. For this purpose, I have constructed a new observable, which gives the probability to find a given number of high-p_{T} recoil jets in events. Presented distribution for recoil jets with $p_{\mathrm{T}} > 30\,\mathrm{GeV}/c$ in HM events with TT$\{20, 30\}$ showed, that probability to find a single jet recoiling from TT in CB is suppressed for such events w.r.t. MB. At the same time, HM events are likely to have a multi-jet configuration. In the wide pseudorapidity region, HM trigger suppresses the probability of having an event without any high-p_{T} recoil jet. The missed single recoil jet can induce HM trigger and cause the suppression of the back-to-back correlation in the Δ_{recoil} observable for HM events w.r.t. MB. The multi-jet events cannot compensate for this loss of jet yield, since the probability of such events is much lower. The same holds concerning jets recoiling from TT$\{6, 7\}$, where we see enhancement of HM events with one jet w.r.t. MB. On average, multi-jet HM events have larger acoplanarity than MB, which is also consistent with the observed broadening of $\Delta_{\mathrm{recoil}}(\Delta\varphi)$ spectra.

We can thus conclude that HM induces bias towards multi-jet events in small systems. This bias must be taken into account in all studies of small collision systems at high multiplicity.

Bibliography

[1] R. Stock, “Relativistic Nucleus-Nucleus Collisions and the QCD Matter Phase Diagram”, doi:10.1007/978-3-540-74203-6–7, arXiv:0807.1610 [nucl-ex].

[2] Heinz U. W., Snellings R. Collective flow and viscosity in relativistic heavy-ion collisions, Annu. Rev. Nucl. Part. Sci. 63 (2013) 123-151, arXiv:1301.2826v1.

[3] A. Majumder and M. Van Leeuwen, “The Theory and Phenomenology of Perturbative QCD Based Jet Quenching”, Prog. Part. Nucl. Phys. **66** (2011), 41-92, doi:10.1016/j.ppnp.2010.09.001, arXiv:1002.2206 [hep-ph].

[4] H. Song, S. A. Bass, U. Heinz, T. Hirano and C. Shen, “Hadron spectra and elliptic flow for 200 A GeV Au+Au collisions from viscous hydrodynamics coupled to a Boltzmann cascade”, Phys. Rev. C **83** (2011), 054910, doi:10.1103/PhysRevC.83.054910, arXiv:1101.4638 [nucl-th].

[5] B. Abelev *et al.* [ALICE], “Long-range angular correlations on the near and away side in p-Pb collisions at $\sqrt{s_{NN}}$ = 5.02 TeV”, Phys. Lett. B **719** (2013), 29-41, doi:10.1016/j.physletb.2013.01.012, arXiv:1212.2001 [nucl-ex].

[6] P.M. Jacobs (for the ALICE Collaboration). Search for jet quenching effects in high multiplicity pp collisions at $\sqrt{s}$ = 13 TeV. Proceedings of the XXVIIIth Conference on Ultrarelativistic Nucleus-Nucleus Collisions (Quark Matter 2019), Wuhan, China. Access mode: https://indico.cern.ch/event/792436/contributions/3538876/.

[7] PYTHIA generator [Electronic source]. Access mode: http://home.thep.lu.se/ torbjorn/pythia81html/Welcome.html.

[8] Yukawa, H. "On the interaction of elementary particles". Proc.Phys.Math.Soc.Jap. 17 (1935) 48-57.

[9] Cesar M. G. Lattes, Giuseppe P. S. Occhialini, Cecil F. Powell, “Observations on the Tracks of Slow Mesons in Photographic Emulsions – Part 1,” Nature 160 (1947a), 453 - 456, idem “Observations on the Tracks of Slow Mesons in Photographic Emulsions. Part 2 – Origin of the Slow Mesons,” Nature 160 (1947b), 486 - 492.

[10] Gell-Mann, M. “The Eightfold Way: A Theory of Strong Interaction Symmetry” (TID-12608). Pasadena, CA: California Inst. of Tech., Synchrotron Laboratory, March 15, 1961, doi: 10.2172/4008239.

[11] Ne’eman, Y. “Derivation of Strong Interactions from a Gauge Invariance”. Nuclear Physics. Amsterdam: North-Holland Publishing Co. 26 (2): 222–229, August, 1961, doi: 10.1016/0029-5582(61)90134-1.

[12] L. Brekke and J. L. Rosner, “Baryon Magnetic Moments in the Quark Model: A Status Report,” Comments Nucl. Part. Phys. **18** (1988) no.2, 83-102 EFI-87-80-CHICAGO.

[13] Jiří Chýla. Quarks, partons and Quantum Chromodynamics. – Institute of Physics, Academy of Sciences of the Czech Republic. Access mode: https://www.fzu.cz/ chyla/lectures/text.pdf.

[14] Wikipedia [Electronic source]. Access mode: https://www.wikipedia.org/.

[15] D.J. Gross; F. Wilczek (1973). “Ultraviolet behavior of non-abelian gauge theories”. Physical Review Letters. 30 (26): 1343 - 1346, doi: 10.1103/PhysRevLett.30.1343.

[16] H.D. Politzer (1973). “Reliable perturbative results for strong interactions”. Physical Review Letters. 30 (26): 1346 - 1349, doi: 10.1103/PhysRevLett.30.1346.

[17] Kovchegov Y., Levin. E. Quantum Chromodynamics at High Energy. – Cambridge University Press, 2012. – 340 pp.

[18] Peskin M., Schroeder D. An Introduction To Quantum Field Theory. – Avalon Publishing, 1995. – 864 pp.

[19] M. Tanabashi et al. (Particle Data Group), Phys. Rev. D 98, 030001 (2018) and 2019 update.

[20] Ian Hinchliffe, Aneesh V. Manohar. The QCD Coupling Constant, Ann.Rev.Nucl.Part.Sci. 50 (2000) 643-678, arXiv:hep-ph/0004186v1.

[21] Peter Braun-Munzinger, Volker Koch, Thomas Schäfer, Johanna Stachel. “Properties of hot and dense matter from relativistic heavy ion collisions”, Physics Reports, Volume 621, 2016, Pages 76-126, ISSN 0370-1573, https://doi.org/10.1016/j.physrep.2015.12.003.

[22] Smilga A. V. Lectures on quantum chromodynamics. – World Scientific, 2001. – 352 pp.

[23] A. Chodos, R. L. Jaffe, K. Johnson, C. B. Thorn, and V. F. Weisskopf Phys. Rev. D 9, 3471 – Published 15 June 1974.

[24] Letessier J. Hadrons and Quark–Gluon Plasma. – Cambridge University Press, 2009. – 398 pp.

[25] Cheuk-Yin Wong. Introduction to High-Energy Heavy-Ion Collisions. – World Scientific, 1994. – 517 pp.

[26] E. Eichten, K. Gottfried, T. Kinoshita, K. D. Lane, and T.-M. Yan, Phys.Rev. D17, 3090 (1978).

[27] Ebert D. , Faustov R. N., Galkin V. O. Mass spectra and Regge trajectories of light mesons in the relativistic quark model, Phys.Rev.D79:114029, 2009, arXiv:0903.5183v2.

[28] Andersson B., Mohanty S., Soderberg F. Recent Developments in the Lund Model, arXiv:hep-ph/0212122v1.

[29] Sourav Sarkar, Helmut Satz, Bikash Sinha. The Physics of the Quark-Gluon Plasma, DOI: https://doi.org/10.1007/978-3-642-02286-9.

[30] G. Wolschin, “Pseudorapidity distributions of produced charged hadrons in pp collisions at RHIC and LHC energies”, EPL **95** (2011) no.6, 61001, doi:10.1209/0295-5075/95/61001, arXiv:1106.3636 [hep-ph].

[31] Wikipedia [Electronic source]. Access mode: https://en.wikipedia.org/wiki/Quark-gluon-plasma.

[32] Aoki Y., Endrodi G., Fodor Z., Katz S.D., Szabo K.K. The order of the quantum chromodynamics transition predicted by the standard model of particle physics, Nature 443:675-678, 2006, arXiv:hep-lat/0611014.

[33] Steinbrecher P. QCD transition at zero and non-zero baryon densities, presentation at the Quark Matter 2018. Access mode: https://indico.cern.ch/event/656452/contributions/2869991/.

[34] Bazavov, A., et al. (HotQCD) (2014), Phys. Rev. D90 (9),094503.

[35] Goy V. A., et al. Sign problem in finite density lattice QCD, Prog Theor Exp Phys (2017) 2017 (3): 031D01, arXiv:1611.08093v2.

[36] Ayala A. et. al. The effective QCD phase diagram and the critical end point, arXiv:1411.4953v2.

[37] Alford M. G. et. al. Color superconductivity in dense quark matter, Rev.Mod.Phys.80:1455-1515, 2008, arXiv:0709.4635v2.

[38] Connors M. et. al. Review of Jet Measurements in Heavy Ion Collisions, Rev. Mod. Phys. 90, 025005 (2018), arXiv:1705.01974v2.

[39] Harris J. W., Müller B. THE SEARCH FOR THE QUARK-GLUON PLASMA, Annual Review of Nuclear and Particle Science Vol. 46:71-107 (Volume publication date December 1996).

[40] Vogt R. Ultrarelativistic Heavy-Ion Collisions, 1st Edition. – Elsevier Science, 2007. – 488 pp.

[41] Snellings R. Elliptic Flow: A Brief Review, New J.Phys.13:055008, 2011, arXiv:1102.3010v2.

[42] P. Huovinen, P. Kolb, U. Heinz, P. V. Ruuskanen and S. A. Voloshin, Phys. Lett. B 503 (2001) 58.

[43] Heinz, Ulrich W. 2005a. 'RHIC serves the perfect fluid': Hydrodynamic flow of the QGP. arXiv:nucl-th/0512051.

[44] Khachatryan, V., Sirunyan, A.M., Tumasyan, A. et al. Observation of long-range, near-side angular correlations in proton-proton collisions at the LHC. J. High Energ. Phys. 2010, 91 (2010). https://doi.org/10.1007/JHEP09(2010)091.

[45] V. Khachatryan *et al.* [CMS], "Long-range two-particle correlations of strange hadrons with charged particles in pPb and PbPb collisions at LHC energies", Phys. Lett. B **742** (2015), 200-224, doi:10.1016/j.physletb.2015.01.034, arXiv:1409.3392.

[46] S. Chatrchyan *et al.* [CMS], "Multiplicity and Transverse Momentum Dependence of Two- and Four-Particle Correlations in pPb and PbPb Collisions", Phys. Lett. B **724** (2013), 213-240, doi:10.1016/j.physletb.2013.06.028, arXiv:1305.0609.

[47] Tung-Mow Yan, Sidney D. Drell. The Parton Model and its Applications. Contribution to a book to be published by World Scientific for the occasion of 50 Years of Quarks, arXiv:1409.0051 [hep-ph].

[48] V.N. Gribov and L.N. Lipatov: Sov. J. Nucl. Phys. 15, 438 (1972) 287.

[49] Butterworth J. M. et. al. KtJet: A C++ implementation of the Kt clustering algorithm, Comput.Phys.Commun. 153 (2003) 85-96, arXiv:hep-ph/0210022v1.

[50] Cacciari M., Salam G. P., Soyez G. FastJet user manual, CERN-PH-TH/2011-297, arXiv:1111.6097v1.

[51] Dissertori G., Knowles I. G., Schmelling M. Quantum Chromodynamics: High Energy Experiments and Theory, – OXFORD SCIENCE PUBLICATIONS, 2009. – 542 pp.

[52] I. Ito, "INFRARED DIVERGENCES IN QCD AND KINOSHITA-LEE-NAUENBERG THEOREM", Prog. Theor. Phys. **67** (1982), 1216, doi:10.1143/PTP.67.1216.

[53] Salam G. P. Towards Jetography, Eur.Phys.J.C67:637-686, 2010, arXiv:0906.1833v2.

[54] Blazey G. C. et. al. Run II Jet Physics: Proceedings of the Run II QCD and Weak Boson Physics Workshop, arXiv:hep-ex/0005012v2.

[55] Campbell J., Huston J., Krauss F. The Black Book of Quantum Chromodynamics: A Primer for the LHC Era, – Oxford: Oxford University Press, 2018. – 749 pp.

[56] Marzani S., Soyez G., Spannowsky M. Looking inside jets: an introduction to jet substructure and boosted-object phenomenology, Lecture Notes in Physics, volume 958 (2019), arXiv:1901.10342v3.

[57] R. Atkin, "Review of jet reconstruction algorithms", J. Phys. Conf. Ser. **645** (2015) no.1, 012008, doi:10.1088/1742-6596/645/1/012008.

[58] S. Catani, Y. L. Dokshitzer, M. H. Seymour and B. R. Webber, Nucl. Phys. B 406 (1993) 187., S. D. Ellis and D. E. Soper, Phys. Rev. D 48 (1993) 3160 [hep-ph/9305266].

[59] S. D. Ellis and D. E. Soper, "Successive Combination Jet Algorithm For Hadron Collisions", Phys. Rev. D 48, 3160 (1993) [hep-ph/9305266].

[60] M. Cacciari, G. P. Salam and G. Soyez, "The Catchment Area of Jets," JHEP **04** (2008), 005, doi:10.1088/1126-6708/2008/04/005, arXiv:0802.1188 [hep-ph].

[61] M. Cacciari, G. P. Salam and G. Soyez, "The anti-k_t jet clustering algorithm," JHEP **04** (2008), 063, doi:10.1088/1126-6708/2008/04/063, arXiv:0802.1189 [hep-ph].

[62] X. N. Wang, Why the observed jet quenching at RHIC is due to parton energy loss, Phys. Lett. B 579.

[63] S. Chatrchyan *et al.* [CMS], "Observation and studies of jet quenching in PbPb collisions at nucleon-nucleon center-of-mass energy = 2.76 TeV", Phys. Rev. C **84** (2011), 024906, doi:10.1103/PhysRevC.84.024906, arXiv:1102.1957 [nucl-ex].

[64] SlidePlayer [Electronic source]. Access mode: https://slideplayer.com/slide/8455537/.

[65] J. Adam *et al.* [ALICE], "Measurement of jet quenching with semi-inclusive hadron-jet distributions in central Pb–Pb collisions at $\sqrt{s_{\mathrm{NN}}}$ = 2.76 TeV", JHEP **09** (2015), 170, doi:10.1007/JHEP09(2015)170, arXiv:1506.03984 [nucl-ex].

[66] S. Acharya *et al.* [ALICE], "Exploration of jet substructure using iterative declustering in pp and Pb–Pb collisions at LHC energies", Phys. Lett. B **802** (2020), 135227, doi:10.1016/j.physletb.2020.135227, arXiv:1905.02512 [nucl-ex].

[67] H. Caines [STAR Collaboration], Jet and Underlying Event Measurements in P+P Collisions at RHIC, Int. J. Mod. Phys. E 20 (2011) 1578, arXiv:1011.4614 [nucl-ex].

[68] M. Cacciari and G. P. Salam, "Pileup subtraction using jet areas", Phys. Lett. B **659** (2008), 119-126, doi:10.1016/j.physletb.2007.09.077, arXiv:0707.1378 [hep-ph].

[69] G. Soyez, "Jet areas as a tool for background subtraction", arXiv:0905.2851 [hep-ph].

[70] Reed R. (for the ALICE collaboration). Full Jet Reconstruction in 2.76 TeV pp and Pb-Pb collisions in the ALICE experiment, arXiv:1304.5945v1.

[71] Abelev, B., et al. (ALICE) (2013d), Phys.Lett. B722, 262.

[72] J. Strologas [CMS],"Performance of Jet reconstruction in CMS at 13 TeV", PoS **ICHEP2016** (2016), 736, doi:10.22323/1.282.0736.

[73] G. Aad *et al.* [ATLAS], "Measurement of the jet radius and transverse momentum dependence of inclusive jet suppression in lead-lead collisions at $\sqrt{s_{NN}}$= 2.76 TeV with the ATLAS detector", Phys. Lett. B **719** (2013), 220-241, doi:10.1016/j.physletb.2013.01.024, [arXiv:1208.1967 [hep-ex]].

[74] C. Nattrass [ALICE], "Measurements of jets in ALICE", J. Phys. Conf. Ser. **589** (2015) no.1, 012015, doi:10.1088/1742-6596/589/1/012015.

[75] F. Křížek [ALICE], "Study of high-p_T hadron-jet correlations in ALICE", J. Phys. Conf. Ser. **805** (2017) no.1, 012013, doi:10.1088/1742-6596/805/1/012013.

[76] G.O.V. de Barros, Bo Fenton-Olsen, Peter Jacobs, Mateusz P loskoń. "Data-driven analysis methods for the measurement of reconstructed jets in heavy ion collisions at RHIC and LHC", Nuclear Physics A, Volumes 910–911, 2013, Pages 314-318, ISSN 0375-9474, https://doi.org/10.1016/j.nuclphysa.2012.12.019.

[77] F. D'Eramo, M. Lekaveckas, H. Liu, and K. Rajagopal, "Momentum Broadening in Weakly Coupled Quark-Gluon Plasma (with a view to finding the quasiparticles within liquid quark-gluon plasma)," JHEP 05 (2013) 031, arXiv:1211.1922 [hep-ph].

[78] F. Carminati *et al.* [ALICE], "ALICE: Physics performance report, volume I", J. Phys. G **30** (2004), 1517-1763, doi:10.1088/0954-3899/30/11/001.

[79] K. Aamodt *et al.* [ALICE], "The ALICE experiment at the CERN LHC", JINST **3** (2008), S08002, doi:10.1088/1748-0221/3/08/S08002.

[80] B. B. Abelev *et al.* [ALICE], "Performance of the ALICE Experiment at the CERN LHC", Int. J. Mod. Phys. A **29** (2014), 1430044, doi:10.1142/S0217751X14300440, arXiv:1402.4476 [nucl-ex].

[81] G. Contin, "Performance of the present ALICE Inner Tracking System and studies for the upgrade", JINST **7** (2012), C06007, doi:10.1088/1748-0221/7/06/C06007.

[82] E. Abbas *et al.* [ALICE], "Performance of the ALICE VZERO system", JINST **8** (2013), P10016, doi:10.1088/1748-0221/8/10/P10016, arXiv:1306.3130 [nucl-ex].

[83] Saint Gobain Crystals, 104 route de Larchant BP 521, 77794 Nemours Cedex, France.

[84] Matteo Cacciari, Juan Rojo, Gavin P. Salam, and Gregory Soyez. Jet Reconstruction in Heavy Ion Collisions. Eur.Phys.J., C71:1539, 2011

[85] G. D'Agostini. A multidimensional unfolding method based on Bayes' theorem. Nuclear Instruments and Methods in Physics Research A, 362:487–498, February 1995.

[86] Kerstin Tackmann, Andreas Höcker. SVD-based unfolding: implementation and experience. – January 20, 2011. Access mode: https://indico.cern.ch/event/107747/contributions/32650/.

[87] RooUnfold: ROOT Unfolding Framework [Electronic source]. Access mode: https://gitlab.cern.ch/RooUnfold/RooUnfold.

[88] T. Sjöstrand, S. Ask, J. R. Christiansen, R. Corke, N. Desai, P. Ilten, S. Mrenna, S. Prestel, C. O. Rasmussen and P. Z. Skands, "An Introduction to PYTHIA 8.2", Comput. Phys. Commun. **191** (2015), 159-177, doi:10.1016/j.cpc.2015.01.024, arXiv:1410.3012 [hep-ph].

[89] PYTHIA Phase Space Cuts, [Electronic source]. Access mode: http://home.thep.lu.se/ torbjorn/pythia82html/PhaseSpaceCuts.html.

[90] PYTHIA Tunes, [Electronic source]. Access mode: http://home.thep.lu.se/ torbjorn/pythia81html/Tunes.html.

[91] P. Skands, S. Carrazza and J. Rojo, "Tuning PYTHIA 8.1: the Monash 2013 Tune", Eur. Phys. J. C **74** (2014) no.8, 3024, doi:10.1140/epjc/s10052-014-3024-y, arXiv:1404.5630 [hep-ph].

[92] TTree Class Reference, [Electronic source]. Access mode: https://root.cern.ch/doc/master/classTTree.html.

[93] S. Acharya *et al.* [ALICE], "Constraints on jet quenching in p-Pb collisions at $\sqrt{s_{NN}}$ = 5.02 TeV measured by the event-activity dependence of semi-inclusive hadron-jet distributions", Phys. Lett. B **783** (2018), 95-113, doi:10.1016/j.physletb.2018.05.059, arXiv:1712.05603 [nucl-ex].

[94] PYTHIA Colour Reconnection, [Electronic source]. Access mode: http://home.thep.lu.se/ torbjorn/pythia82html/ColourReconnection.html.

[95] J. C. Collins and M. Perry, “Superdense Matter: Neutrons Or Asymptotically Free Quarks?”, Phys. Rev. Lett. **34** (1975), 1353, doi:10.1103/PhysRevLett.34.1353.